Numerical failure analysis of a stretch-bending test on dual-phase steel sheets using a phenomenological fracture model

Citation: Luo, Meng, and Tomasz Wierzbicki. "Numerical Failure Analysis of a Stretch-Bending Test on Dual-Phase Steel Sheets Using a Phenomenological Fracture Model." International Journal of Solids and Structures 47, no. 22–23 (November 2010): 3084–3102. © 2010 Elsevier Ltd.

As Published: http://dx.doi.org/10.1016/j.ijsolstr.2010.07.010

Publisher: Elsevier

Persistent URL: http://hdl.handle.net/1721.1/96040

Version: Final published version: final published article, as it appeared in a journal, conference proceedings, or other formally published context

International Journal of Solids and Structures 47 (2010) 3084–3102

Contents lists available at ScienceDirect

International Journal of Solids and Structures

journal homepage: www.elsevier.com/locate/ijsolstr

Numerical failure analysis of a stretch-bending test on dual-phase steel sheets using a phenomenological fracture model

Meng Luo *, Tomasz Wierzbicki

Impact and Crashworthiness Lab, Massachusetts Institute of Technology, Cambridge, MA 02139, USA

ARTICLE INFO

Article history:
Received 21 December 2009
Received in revised form 31 May 2010
Available online 21 July 2010

Keywords:
Ductile fracture
Advanced High Strength Steels (AHSS)
Stretch-bending
Modified Mohr–Coulomb
Stamping
Shear fracture

ABSTRACT

Advanced High Strength Steels (AHSS) are increasingly used in automotive industry due to their superior strength and substantial weight advantage. However, their compromised ductility gives rise to numerous manufacturing issues. One of them is the so-called 'shear fracture' often observed on tight radii during stamping processes. Since traditional approaches, such as the Forming Limit Diagram (FLD), are unable to predict this type of fractures, great efforts have been made to develop failure criteria that could predict shear fractures. In this paper, a recently developed Modified Mohr–Coulomb (MMC) ductile fracture criterion (Bai and Wierzbicki, 2010) is adopted to analyze the failure behavior of a Dual Phase (DP) steel sheet during stretch-bending operations. The plasticity and ductile fracture of the present sheet are fully characterized by a Hill'48 orthotropic model and a MMC fracture model, respectively. Finite element models with three different element types (3D, shell and plane strain) were built for a Stretch Forming Simulator (SFS) test (Shih and Shi, 2008), numerical simulations with four different R/t values (die radius normalized by sheet thickness) were performed. It has been shown that the 3D and shell element simulations can predict failure location/mode, the upper die load–displacement responses as well as wall stress and wrap angle at the onset of fracture for all R/t values with good accuracy. Furthermore, a series of parametric studies were conducted on the 3D element model, and the effect of tension level (clamping distance), tooling friction, mesh size and fracture locus on failure modes and load–displacement responses were investigated.

1. Introduction

The use of Advanced High Strength Steels (AHSS) in automotive industry has increased dramatically over the past decade due to their great potential for reducing car weight and enhancing crashworthiness. The mechanical properties of these steels are usually tuned by altering their microstructures, especially the martensite volume fraction, which features high strength but low ductility. Therefore, while industry keeps chasing higher strength, the formability of AHSS is compromised. Various issues have arisen during the manufacturing processes of AHSS. A typical problem that has been widely seen in press shops is the fracture occurring on tight punch/die radii in stamping processes. This type of fracture is oriented perpendicular to the stretching direction in-plane, exhibits little localized necking, presents 45° slant crack through thickness, and is thus termed 'shear fracture' in the forming industry.

The process of bending sheet metal over a radius with superimposed tension is recognized as an important deformation mode for sheet metal. Marciniak and Duncan (1992) analyzed the problem for different material models, and they developed a special equipment for stretch-bending metal strips known as a Modified Duncan–Shabel (MDS) apparatus (Walp et al., 2006). Recently, the forming community has shown great interest in this area due to the shear fracture issue in AHSS stamping. An important thrust on studies of the sheet metal stretch-bending is the fact that traditional formability measures, such as Forming Limit Diagram (FLD), fails to predict shear fracture at tight punch/die radii (Sriram et al., 2003). Consequently, great efforts have been made in order to find an alternative approach to predict such fractures. On the experimental side, Gotoh et al. (1997) conducted a series of draw-bending tests on Cu-0, and showed a clear transition from shear fracture on die radii to tensile failure on the side wall as the R/t (die/punch radii to sheet thickness) ratio increases. Also, continuous efforts have been made in the forming industry to correlate failure stress (or other similar index) to R/t ratio and thus obtain empirical critical R/t ratios of shear fracture for various AHSS by conducting MDS or similar tests (Sriram et al., 2003; Walp et al., 2006; Shih and Shi, 2008; Levy and Van Tyne, 2009; Shih et al., 2009; Shih, 2009). On the analytical side, Bai and Wierzbicki (2008) derived close-form solution for both global force responses and local strain and stress state in the MDS stretch-bending test assuming plane strain

* Corresponding author. Tel.: +1 617 386 3325.
E-mail address: mengluo@mit.edu (M. Luo).

0020-7683/$ - see front matter © 2010 Elsevier Ltd. All rights reserved.
doi:10.1016/j.ijsolstr.2010.07.010

condition. Issa (2009) extended Bai's solution by incorporating power hardening law and considering loading history. However, only few numerical works can be found in the literatures (Bai and Wierzbicki, 2008; Kim et al., 2009; Wagoner et al., 2009). Clearly, considering the incompetence of FLD, a reliable numerical method for failure prediction in the stretch-bending case is still under high demand from the forming community. Here, we adopt a ductile fracture approach, form a detailed numerical procedure from plasticity to fracture, and then validate the model by simulating a real stretch-bending operation on a dual-phase steel sheet.

In order to choose a proper ductile fracture model for the problem at hand, a brief review of the existing models is necessary. From a microscopic point of view, the basic mechanism of ductile fracture is void growth, nucleation and coalescence. In this regard, a large volume of the ductile fracture studies focus on the relationship between plastic distortion and micro-void evolution. Over the past four decades, there emerged numerous micro-mechanics based fracture models, in which pressure (or stress triaxiality η) is a key ductility-controlling parameter. These works include both classical formulations (McClintock, 1968; Rice and Tracey, 1969; Gurson, 1975; Tvergaard and Needleman, 1984) and recent developments (Leblond et al., 1995; Pardoen and Hutchinson, 2000; Benzerga et al., 2004; Nahshon and Hutchinson, 2008). Meanwhile, macroscopically, the damage induced by micro-voids can also be modeled by manipulating local stress and strain components. Consequently, a family of continuum damage mechanics models has been developed under thermodynamic framework (Lemaitre, 1985; Chaboche, 1988a,b; Voyiadjis and Dorgan, 2007). From an industry point of view, the increasing demand for numerical simulations of sheet metal forming processes and vehicle collisions calls for an accurate fracture model which can be easily calibrated from physical tests and efficiently implemented into FE codes. Apparently, most of the above-mentioned fracture models do not meet this requirement. For instance, Gurson-like physically based models usually have too many coefficients to be determined and most of AHSS are not even porous. The fully-coupled damage mechanics approach does not have a solid physical basis in crack formation mechanisms, and the dissipation potential used for damage evolution is not well established for practical use. Therefore, one can see a clear demand for a model that can achieve a balance between the complexity of the underlying physics and the simplicity needed for practical industrial applications.

Under aforementioned concerns, phenomenological models appear to be most suitable for industrial applications. It is usually postulated that the fracture initiates when the weighted accumulative equivalent plastic strain reaches a critical value C (Bao and Wierzbicki, 2004),

$$\int_0^{\bar{\varepsilon}_f} w(\underline{\sigma}) d\bar{\varepsilon}_p = C \tag{1}$$

where w is a weighting function of Cauchy stress tensor $\underline{\sigma}$ or its invariants, accounting for the effect of stress state on ductile fracture, $\bar{\varepsilon}_p$ denotes the equivalent plastic strain, and $\bar{\varepsilon}_f$ represents equivalent strain to fracture (or fracture strain for short). Bao and Wierzbicki (2004) performed a comparative study on eight models of this class, featuring weighting functions from McClintock (1968), Rice and Tracey (1969), Leroy et al. (1981), Clift et al. (1990) and the modified Cockcroft and Latham criterion (1968) by Oh et al. (1979). They analyzed the applicability of each model and proposed a three-branch weighting function that works over a large range of stress triaxiality η. While classical ductile fracture models use η (or pressure) as the only stress state parameter controlling ductility, recent studies (Zhang et al., 2001; Kim et al., 2004; Coppola et al., 2009) have shown that ductile fracture limit also depends on the deviatoric stress state, represented by the Lode parameter. Xue (2007a,b) introduced the Lode parameter into the weighting function and formed a more general ductile fracture model incorporating the effect of all three stress invariants on damage evolution. Recently, Bai and Wierzbicki (2010) obtained a novel weighting function by transforming the classical stress-based Mohr–Coulomb failure criterion into the space of stress triaxiality, Lode parameter and equivalent plastic strain. The resulting phenomenological ductile fracture model is called 'Modified Mohr–Coulomb' (MMC) model, which can predict both triaxiality and Lode angle dependence. This model is an extension of the maximum shear stress fracture criterion and is thus well poised to predict shear fracture which has been shown to be a major failure mode of sheet metal under various loading conditions. Moreover, the MMC criterion has only three free parameters to be calibrated and is thus an ideal choice for industrial applications (Luo and Wierzbicki, 2009; Li et al., 2010). Consequently, in this study, the MMC fracture is the model of choice to capture the failure behavior of the AHSS sheets in stretch-bending operations.

In this paper, the plastic behavior and ductile fracture property of a DP780 sheet are shown to be fully characterized by Hill's (1948) orthotropic plasticity model and MMC fracture model, respectively. A numerical procedure for both plasticity and fracture is developed and implemented into commercial FE software through a user material subroutine in Abaqus Explicit. Detailed FE simulations of a quasi-static stretch-bending operation are carried out with the calibrated models. The comparisons of both global punch load–displacement responses and fracture location with recently published experimental results prove the accuracy and validity of the present method. Finally, a series of parametric studies are conducted to investigate the effect of punch/die friction, tension level, mesh size and fracture envelope on the failure behavior in a stretch-bending process.

2. Material and plasticity

2.1. Material

The family of AHSS is comprised of a variety of steel grades, most of which are multiphase materials with tensile strengths of 600 MPa and higher, such as Dual Phase (DP), Transformation Induced Plasticity (TRIP), and Complex Phase (CP). In this paper, a 1 mm-thick dual-phase steel sheet with 780 MPa minimum tensile strength (DP780) provided by US Steel Corporation is chosen for our study. DP steel features a microstructure consisting of a soft ferrite matrix and islands of martensite as the secondary phase. The martensite volume fraction (MVF) of the present DP780 sheet is about 30%.

2.2. Plasticity characterization

A complete plasticity model is comprised of a yield surface, the flow rule and a hardening law. In the literature, various yield surfaces have been employed to model AHSS: von Mises isotropic yield surface (Yoshida et al., 2000; Durrenberger et al., 2008); Hill's (1948) quadratic orthotropic yield function (Banu et al., 2006; Chen and Koc, 2007); non-quadratic anisotropic Barlat et al. (2003) yield surface (Lee et al., 2005). Here, we make use of the Hill'48 orthotropic yield surface, with the associated flow rule and the isotropic hardening law to model the DP780 sheet. The yield condition reads

$$f(\underline{\sigma}, \bar{\varepsilon}^p) = \bar{\sigma}_{Hill} - s = 0 \tag{2}$$

$$\bar{\sigma}_{\text{Hill}} = \sqrt{F(\sigma_y - \sigma_z)^2 + G(\sigma_z - \sigma_x)^2 + H(\sigma_x - \sigma_y)^2 + 2L\tau_{yz}^2 + 2M\tau_{zx}^2 + 2N\tau_{xy}^2} \tag{3}$$

where $\bar{\sigma}_{\text{Hill}}$ is the Hill'48 equivalent stress, $\bar{\varepsilon}^{\text{p}}$ denotes its corresponding work-conjugate equivalent plastic strain, $\underline{\sigma}$ represents the Cauchy stress tensor, and s is the deformation resistance usually governed by a hardening law (Eq. (5)). The six constants F–N are measures of anisotropy, and can be calculated from the Lankford ratios r assuming associated flow rule. The associated/normality flow rule of Hill'48 yield function can be written as

$$d\underline{\varepsilon}^{\text{p}} = d\bar{\varepsilon}^{\text{p}} \frac{\partial f}{\partial \underline{\sigma}} \tag{4}$$

where $\underline{\varepsilon}^{\text{p}}$ is the plastic strain tensor.

Uniaxial tensile tests were conducted to identify the plasticity parameters. Two dog-bone shaped specimens with a 50 mm long and 12.5 mm wide gauge section were cut from each of three different sheet orientations (0°, 45°, 90° to the rolling direction). The engineering stress–strain curves up to the onset of necking (maximum load) from six tests are shown in Fig. 1. It is found that the stress–strain curves from 0° and 90° direction are almost identical, while the curves from 45° direction are slightly lower (up to 3%). An average Lankford ratio of $r = 0.8$ from six uniaxial tensile tests were measured using Digital Image Correlation (DIC). Only small variation (5%) of this ratio was observed with respect to sheet orientation. Therefore, based on the experimental observations, it is safe to assume that the present DP780 sheet is planar isotropic. Using the average Lankford ratio, one can readily calculate the corresponding Hill's constants in Eq. (3) (Abaqus, 2009). The values of Lankford and Hill's parameters of the present steel sheet are summarized in Table 1.

Hardening rule is also a key ingredient of the plasticity model. The true stress–strain curve up to the necking point (true strain 0.1) for a 0° specimen is shown in Fig. 2a, and the Swift law

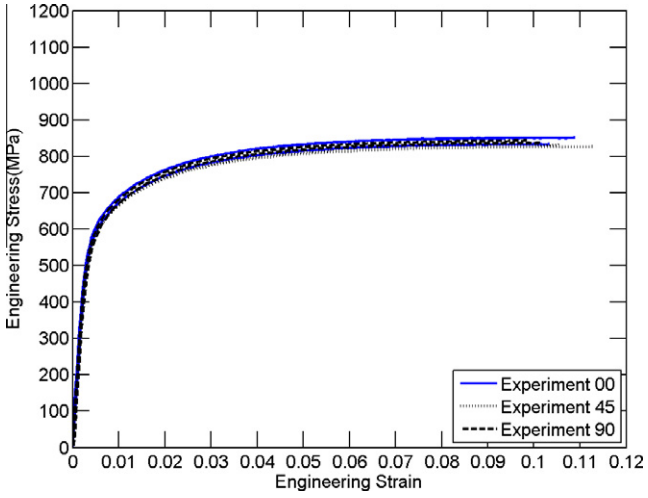

Fig. 1. Engineering stress–strain curves from uniaxial tensile tests on three DP780 sheet orientations.

Table 1
Lankford ratio and Hill's constants of DP780 steel sheets.

Lankford ratio r	Hill'48 constants					
	F	G	H	L	M	N
0.8	0.56	0.56	0.44	1.5	1.5	1.5

$$s = A(\varepsilon_0 + \bar{\varepsilon}^{\text{p}})^n \tag{5}$$

provides a good fit for the true stress–strain curve during the stage of uniform elongation (see Table 2 for hardening parameters). However, for true strain exceeding 0.1, a localized neck develops and the Swift law fitting must be modified. Here, an inverse method is utilized to obtain a reliable stress–strain relation beyond necking. A detailed FE model (0.3 mm × 0.3 mm × 0.3 mm solid mesh in gauge section) was built for the uniaxial tensile test in Abaqus Explicit, and the Hill'48 plasticity and associated flow rule were implemented through a user material subroutine. The element size of this FE model was determined following the same procedure as in the article by Dunand and Mohr (2010), and it was set to the value below which the FE solution converges. As shown in Fig. 2, in simulations of the test, by manually optimize the post-necking part of the Swift law hardening curve (three red[1] diamonds in Fig. 2a), one can get a corrected hardening curve (black dashed line with circles in Fig. 2a) which can give a much better load–displacement response prediction than the Swift law, see Fig. 2b. The final hardening curve is a combined one with Swift law before necking and corrected piece-wise linear curve beyond necking. Both the Swift law parameters and the piece-wise post-necking data are listed in Table 2. A similar approach was used by Mohr and Ebnoether (2009).

2.3. Plasticity validation

The strips in the stretching bending operations are mostly under a stress state that is between uniaxial tension and plane strain tension. As shown in Fig. 9, the strip portion on a tight die radius is usually under plane strain bending, while the strip between clamped ends and the radii is close to uniaxial tension. Therefore, an ideal plasticity model for such applications should at least give good prediction for these two stress states. Fig. 3 shows the plane stress yield surfaces for DP780 of both von Mises and Hill'48 (with $r = 0.8$) models. The black dot denotes the uniaxial tension state, the squares represent the plane strain tension condition, so the red[2] curves between the dot and squares are the stress states between uniaxial and plane strain tension, which are of special interest to this study. The stress paths between the origin and the three stress states at initial yield are strictly linear and denoted by green[2] arrows in Fig. 3. The performance of the Hill'48 plasticity model under uniaxial tension has been shown in Fig. 2b. Here, we validate it under plane strain condition, on which von Mises and Hill'48 show a considerable difference in Fig. 3.

The test results of Walters (2009) on a butterfly shaped specimen (Fig. 4a) are used for this plane strain validation. Under pure tension, this full-thickness plasticity specimen features a uniform plane strain condition in its gauge section. A FE model of this plane strain tension test was built in Abaqus Explicit (Fig. 4b), and both von Mises and Hill'48 plasticity model were implemented to describe the plastic responses. As shown in Fig. 5, the Hill'48 model provides a perfect prediction of the load–displacement relation, while the von Mises one overestimates the force level. Therefore, the present plasticity model with Hill'48 yield function, the associated flow rule and the isotropic hardening law has been validated for both uniaxial tension and plane strain tension condition, and thus is competent for the stretch-bending simulations.

[1] For interpretation of the references to color in Fig. 2, the reader is referred to the web version of this paper.

[2] For interpretation of the references to color in Fig. 3, the reader is referred to the web version of this paper.

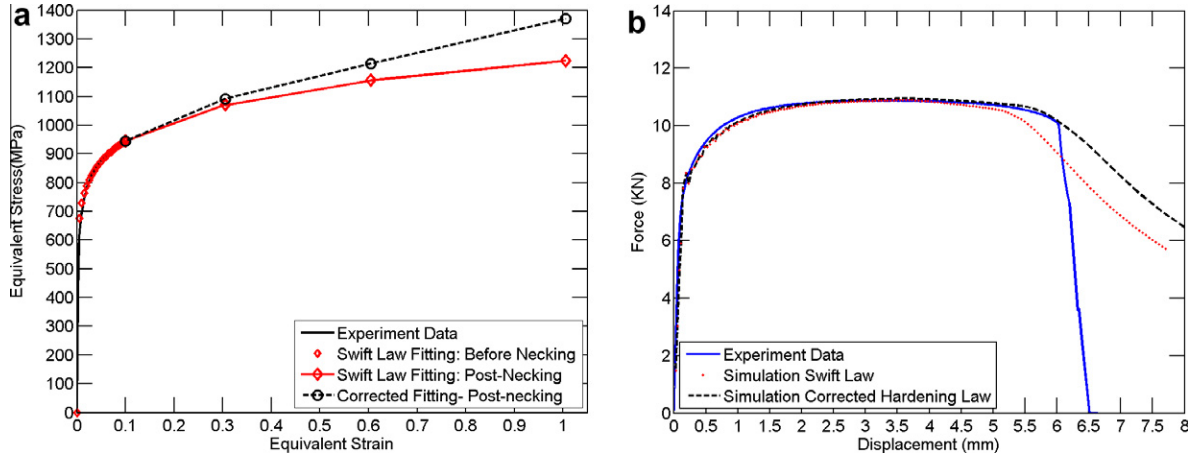

Fig. 2. Identification of a reliable hardening law: (a) Swift law fitting and the corrected post-necking hardening curve; (b) load–displacement prediction of both hardening curves (gauge length = 31.4 mm).

Table 2
Corrected hardening curve.

True strain level	ε = 0–0.1 Uniform elongation	ε = 0.1–1 Post-necking		
		ε = 0.3	ε = 0.6	ε1.0
Deformation resistance s	Swift law: A = 1223 MPa ε_0 = 0.003 n = 0.11	1091.9 MPa	1214 MPa	1371 MPa

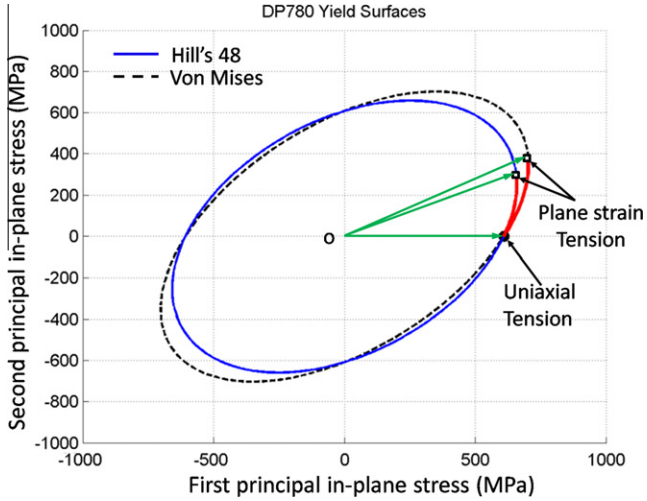

Fig. 3. Planar isotropic Hill'48 initial yield surface for r = 0.8 with superimposed von Mises yield surface of DP780 sheet.

3. Fracture modeling

3.1. Characterization of stress states

As introduced in Section 1, a phenomenological fracture model usually features a weighting function for the accumulated equivalent plastic strain (Eq. (1)). It is normally a function of stress tensor or stress invariants, and it can describe the effect of stress state on the micro-void evolution or damage accumulation macroscopically. In this study, a phenomenological MMC model with both stress triaxiality (pressure) and Lode angle dependence is adopted and calibrated to simulate the stretch-bending operation. Hence, a characterization of stress states in terms of triaxiality and Lode angle parameter is necessary.

The first invariant of Cauchy stress tensor (I_1) and the second and third invariants of the Cauchy stress deviator (J_2,J_3) are defined as:

$$I_1 = \mathrm{tr}(\underline{\sigma}) \tag{6}$$

$$J_2 = \frac{1}{2}\underline{S} : \underline{S} \tag{7}$$

$$J_3 = \det(\underline{S}) \tag{8}$$

where $\underline{S}$ denotes the deviatoric Cauchy stress tensor,

$$\underline{S} = \underline{\sigma} - \frac{1}{3} I_1 \underline{1} \tag{9}$$

where $\underline{1}$ is the identity tensor. The hydrostatic pressure p and mean stress σ_m are related to I_1 through

$$p = -\sigma_m = -\frac{1}{3} I_1 \tag{10}$$

The second invariant J_2 is related to von Mises equivalent stress defined as

$$\bar{\sigma}_{\text{Mises}} = \sqrt{3J_2} \tag{11}$$

It is convenient to work with the dimensionless hydrostatic pressure η, which is defined as

$$\eta = \frac{-p}{\sqrt{3J_2}} = \frac{\sigma_m}{\bar{\sigma}_{\text{Mises}}} \tag{12}$$

The parameter η is the famous stress triaxiality parameter, which has been extensively used in the literature for ductile fracture (McClintock, 1968; Rice and Tracey, 1969; Hancock and Mackenzie, 1976; Johnson and Cook, 1985; Bao, 2003). Another key parameter is the Lode angle θ, which is related to the normalized J_3 through

$$\theta = \frac{1}{3}\cos^{-1}\left(\frac{3\sqrt{3}}{2}\frac{J_3}{J_2^{3/2}}\right)\left(0 \leqslant \theta \leqslant \frac{\pi}{3}\right) \tag{13}$$

The dimensionless Lode angle parameter $\bar{\theta}$ is often defined as

$$\bar{\theta} = 1 - \frac{6\theta}{\pi}\left(-1 \leqslant \bar{\theta} \leqslant 1\right)$$

It can be seen that η and θ incorporate the effect of all three invariants and thus are good representations of stress states. Furthermore, σ_m, $\bar{\sigma}_{\text{Mises}}$ and θ define the cylindrical Haigh–Westergaard coordinate system which can represent all stress states. Readers are

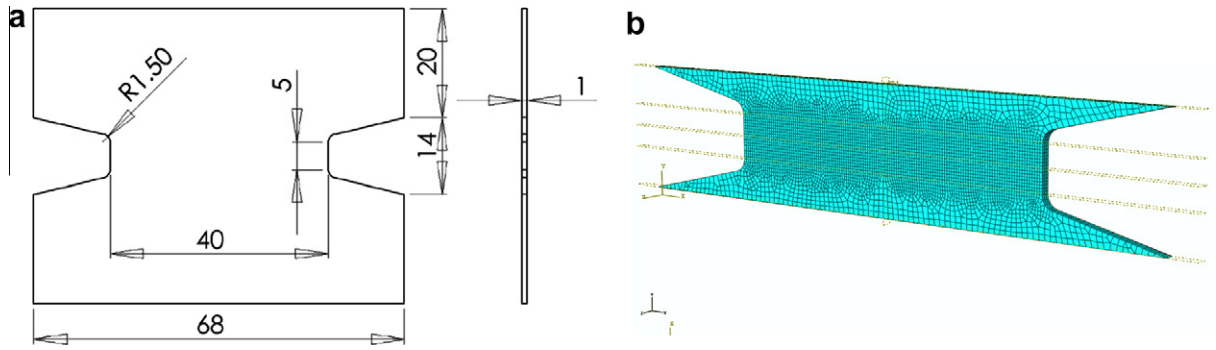

Fig. 4. The plane strain plasticity specimen: (a) drawing with dimension (Walters, 2009); (b) FE model of the specimen gauge section, with three solid elements through thickness.

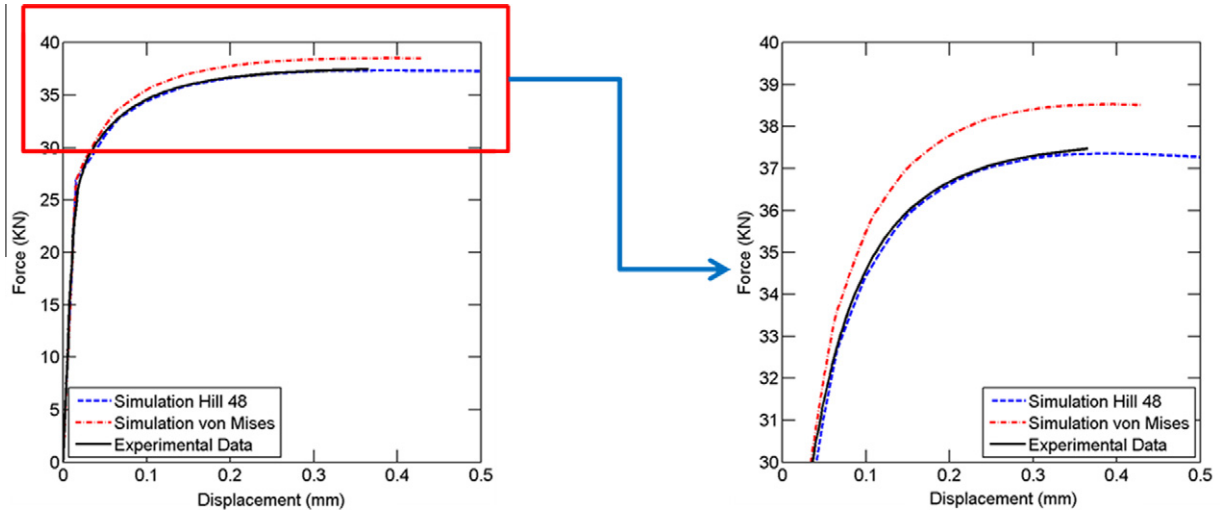

Fig. 5. Comparison of the plane strain tension load–displacement curves predicted by numerical simulations against experimental data (gauge length = 5 mm).

referred to Bai and Wierzbicki (2010) and Coppola et al. (2009) for detailed geometric representations.

3.2. Phenomenological MMC ductile fracture model

A typical interpretation of the phenomenological ductile fracture criteria is to rewrite Eq. (1) as

$$D = \int_0^{\bar{\varepsilon}_f} \frac{d\bar{\varepsilon}_p}{\hat{\varepsilon}_f(\eta,\bar{\theta})} = C = 1 \tag{14}$$

where the integral of the weighted accumulative equivalent plastic strain is referred to as a damage indicator D, and the weighting function $\hat{\varepsilon}_f(\eta,\bar{\theta})$ is usually termed as a 'fracture envelope', which defines the fracture strain of the material under all possible proportional stress states. Eq. (14) says that a given increment of the equivalent plastic strain $d\bar{\varepsilon}_p$ contributes to the damage accumulation in a linear incremental way depending on the current stress state $(\eta,\bar{\theta})$. It should be pointed out that the so-called 'damage' in the present framework is a mathematical or phenomenological artifice aiming to describe the loss of material ductility. It is not explicitly related to any microscopic representative volume, nor coupled with plasticity, but is meant to model the microscopic damage in a macroscopic way. Also, it is postulated that fracture will initiate when its limit of ductility is reached, and $D = C = 1$. Therefore, with the framework established, the major task would be finding an appropriate functional form of $\hat{\varepsilon}_f(\eta,\bar{\theta})$.

As mentioned in Section 1, Bai and Wierzbicki (2010) derived a novel functional form of the MMC fracture envelope by transforming the classical stress-based Mohr–Coulomb failure criterion into the space of stress triaxiality, Lode angle parameter and equivalent plastic strain. The functional form of MMC fracture envelope reads

$$\hat{\varepsilon}_f = \left\{\frac{A}{c_2}\left[c_3 + \frac{\sqrt{3}}{2-\sqrt{3}}(1-c_3)\left(\sec\left(\frac{\bar{\theta}\pi}{6}\right)-1\right)\right] \times \left[\sqrt{\frac{1+c_1^2}{3}}\cos\left(\frac{\bar{\theta}\pi}{6}\right) + c_1\left(\eta + \frac{1}{3}\sin\left(\frac{\bar{\theta}\pi}{6}\right)\right)\right]\right\}^{-\frac{1}{n}} \tag{15}$$

where the fracture strain under proportional loading is a function of triaxiality η and normalized Lode angle $\bar{\theta}$, A and n are Swift law hardening parameters, and c_1, c_2, c_3 are three material constants which should be calibrated through as few as three lab-based fracture tests. As shown in Fig. 6a, the geometric representation of the MMC fracture envelope is 3D half-tube which is asymmetric with respect to $\bar{\theta} = 0$, and both triaxiality (pressure) and Lode angle dependence can be predicted by this envelope.

For sheet metal applications where plane stress condition prevail, a unique relationship between triaxiality and Lode angle has been obtained by Wierzbicki and Xue (2005)

$$-\frac{27}{2}\eta\left(\eta^2 - \frac{1}{3}\right) = \cos(3\theta) = \sin\left(\frac{\pi}{2}\bar{\theta}\right) \tag{16}$$

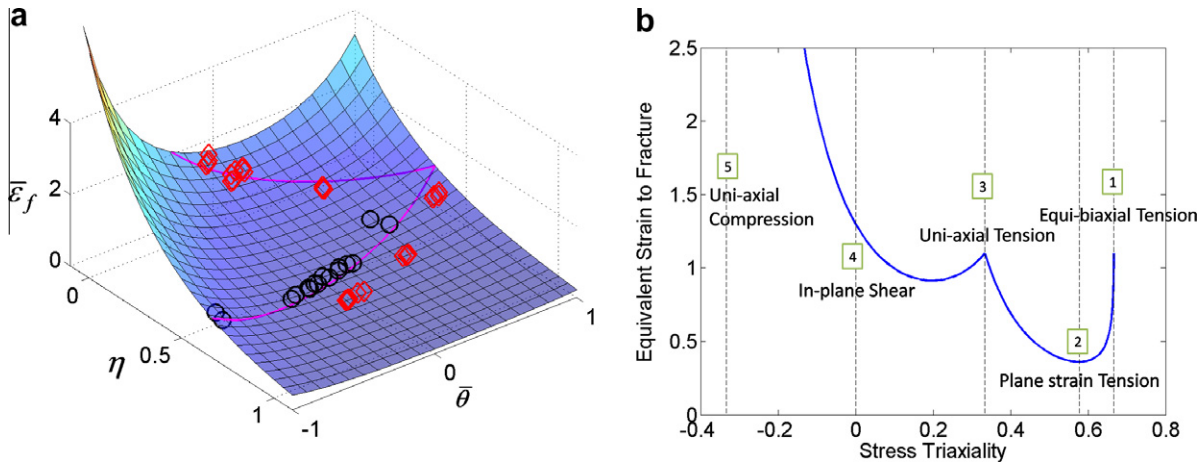

Fig. 6. The MMC fracture envelopes for DP780: (a) general 3D envelope; (b) 2D envelope for plane stress condition.

Eliminating $\bar{\theta}$ between Eqs. (15) and (16), one can obtain a 2D plane stress fracture envelope depending only on stress triaxiality (Beese et al., 2010). Fig. 6b shows the shape of the 2D fracture envelope, and it can be seen that it is simply the projection of a trajectory on the general 3D envelope (pink[3] line in Fig. 6a) onto the $(\hat{\varepsilon}_f, \eta)$ plane, where that trajectory satisfies Eq. (16).

With the fracture envelope well defined, the fracture criterion employed in this study takes the form

$$D = \int_0^{\bar{\varepsilon}_f} \frac{d\bar{\varepsilon}_p}{\hat{\varepsilon}_f(\eta, \bar{\theta})} = 1 \tag{17}$$

where the weighting function is defined by Eq. (15).

3.3. Fracture calibration

Fracture calibration is essentially to determine the three free parameters c_1, c_2, c_3 in Eq. (15) through experiments. The experimental fracture calibration makes use of the fracture envelope Eq. (15). Since fracture envelope is a locus of fracture strains attainable for all proportional loadings, the experimental calibration calls for fracture tests which feature almost constant triaxiality and Lode angle level all the way to fracture. With at least three different tests providing three unique combinations of η and $\bar{\theta}$, one can get independent experimental points in the space of fracture envelope $(\eta, \bar{\theta}, \hat{\varepsilon}_f)$, then various optimization approaches could be taken to fit the fracture envelope to the experimental points and thus obtain c_1, c_2 and c_3.

For the present DP780 sheet, significant effort has been made to develop lab-based fracture testing techniques by Walters (2009). Sixteen Hasek (1978) punch tests (black circles in Fig. 6a) and 32 biaxial butterfly specimen tests (red[3] diamonds in Fig. 6a) were conducted all the way to fracture, and all these tests have small variation on their stress states during the whole loading process. The stress state parameters η and $\bar{\theta}$ for each test were obtained through detailed FE simulations, and the Hill'48 equivalent strain to fracture for every test was determined by a hybrid method of DIC and FEA. Detailed information about fracture testing can be found in Walters (2009). All the test points are plotted in $(\eta, \bar{\theta}, \hat{\varepsilon}_f)$ space in Fig. 6a, and a Matlab subroutine was written to minimize the Mean Squared Error (MSE) between test results and fracture envelope and optimize the values of c_1, c_2 and c_3. The calibrated MMC parameters are listed in Table 3, and one can see a small MSE value of 5.7% for 48 tests, which shows a strong data fitting ability of the MMC fracture envelope. The calibrated 3D fracture envelope is shown in Fig. 6a, and its plane stress 2D envelope is displayed in Fig. 6b.

Table 3
Calibrated MMC parameters of DP780 and mean squared error for the calibration.

Material	Calibrated MMC parameters			MSE
	c_1	c_2	c_3	
DP780	0.1535	720 MPa	0.9792	5.7%

The 2D plane stress fracture envelope is handy for sheet metal applications. As shown in Fig. 6b, the envelope consists of four branches separated by five typical stress states for sheets. Assuming proportional loading and associated flow rule, the 2D MMC fracture envelope can be readily transformed into a Fracture Forming Limit Diagram (FFLD) (Bai, 2008), see Fig. 7. An experimentally determined FLD of DP780 is also superimposed in Fig. 7, and it can be seen that the FFLD is higher than FLD. This discrepancy is due to the fact that the FLD was measured using standard industrial method by measuring in-plane strains before necking with a length scale of 2.54 mm, while FFLD was calibrated using local fracture strains measured inside the neck using DIC and FE inverse method with length scale of about 0.03 mm. Furthermore, FFLD can cover the stress states between uniaxial tension and compression which could not be predicted by FLD. Moreover, in the present framework, the MMC fracture envelope is not used simply as a strain limit, but as a reference strain value in the damage accumulation rule (Eq. (17)). This scheme enables its applicability for non-proportional loading conditions, where FLD usually does not work.

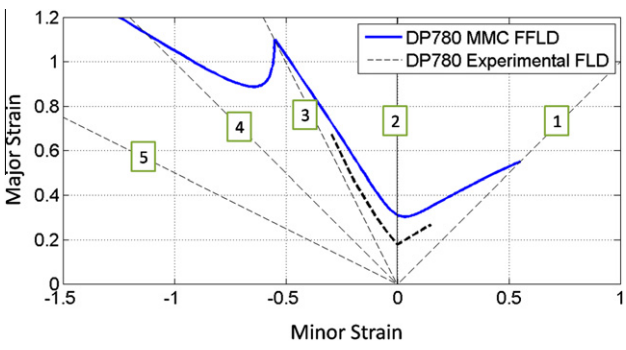

Fig. 7. MMC fracture Forming Limit Diagram with superimposed FLD (courtesy of US Steel Corporation).

[3] For interpretation of the references to color in Fig. 6, the reader is referred to the web version of this paper.

4. Experimental procedures for stretch-bending

Shih and Shi (2008) and Shih et al. (2009) performed full sets of stretch-bending tests with a Stretch Forming Simulator (SFS) on various AHSS strips, including the present DP780 steel. As shown in Fig. 8, the SFS provides an ideal lab-based testing environment for the first stage of a typical automotive stamping process (Fig. 9), where shear fracture periodically occurs. During a SFS test, the strip is first clamped on both sides, and then the upper die moves down and stretches the blank into the die cavity, while both the tension level within the strip and the wrap angle ϕ increase.

It has been widely reported (Walp et al., 2006; Hudgins et al., 2007; Shih and Shi, 2008; Shih et al., 2009) that the failure modes in the stretch-bending operations are determined by the combination of R/t ratio and the applied tension level on the sheet. In a SFS test, the R/t ratio can be altered by replacing different lower dies, and the tension level on the strip is controlled by adjusting the clamping distance d, see Fig. 8. The radius of the upper die is fixed at a relatively large value (18 mm), so the failure modes of the strips under SFS testing are limited to three cases:

(1) Shear fracture within lower die radius (Fig. 10a).
(2) Mixed failure on the tangent point between lower die radius and sidewall (Fig. 10b).
(3) Tensile failure in the sidewall between upper and lower dies (Fig. 10c).

Normally, the fractured surface is perpendicular to the strip axis except when fracture occurs on the side wall. Fig. 11 gives a good example of this phenomenon. On the side wall, the state of stress is almost uniaxial, and the fracture occurs either diagonally or in a zigzag way. In those cases, the fracture location was defined as the initiation site of the fracture, which is usually in the middle of the strip.

In addition to the failure mode/location, other test results that are of great interest to the forming community include the wall stress σ_w at failure (load along sidewall normalized by original cross-sectional area), wrap angle ϕ at failure and drawing depth h at failure, see Fig. 9b.

For this study, the test results from US Steel Corporation (Shih and Shi, 2008; Shih et al., 2009; Shih, 2009) on 2-in.-wide

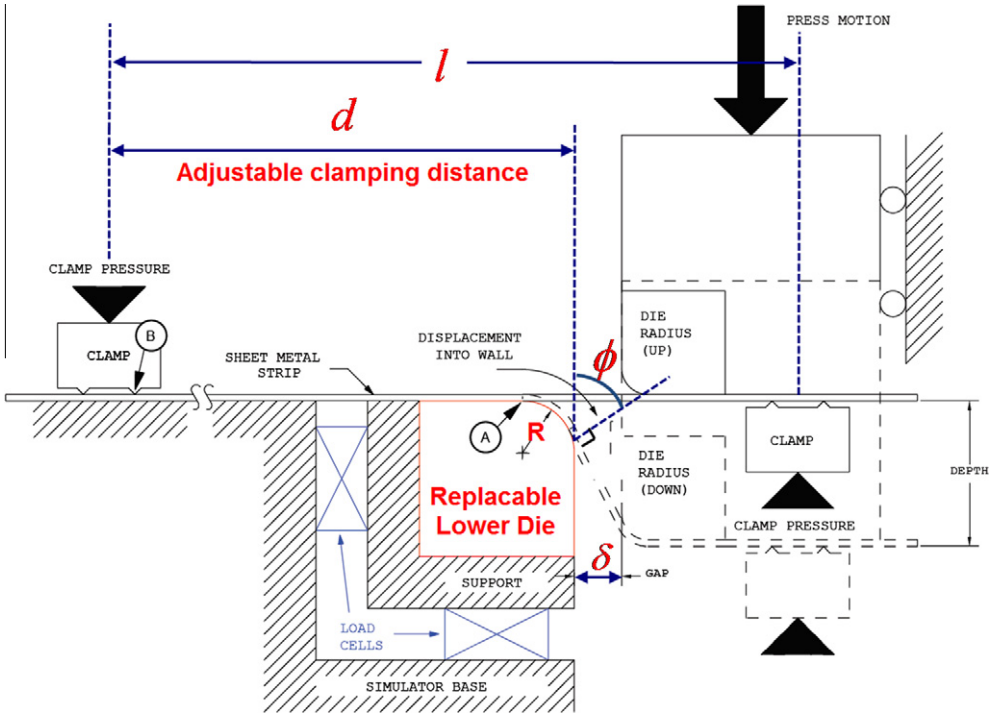

Fig. 8. Schematic drawing of the SFS test (Shih et al., 2009).

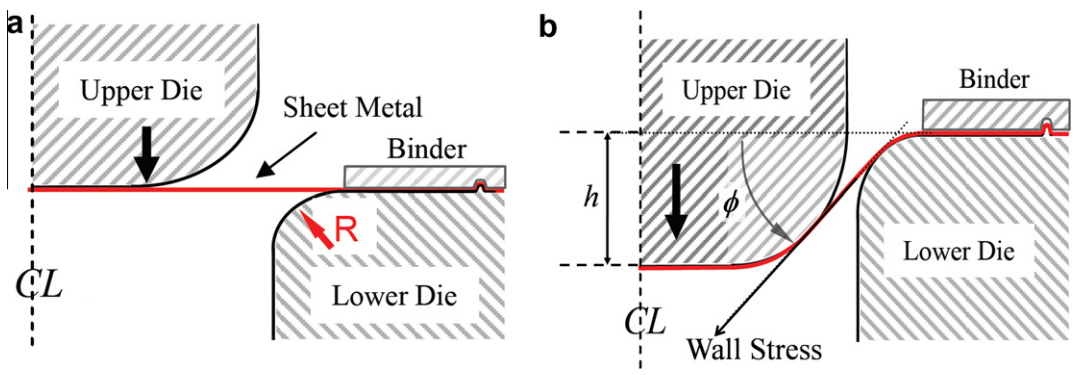

Fig. 9. Typical first stage of a stamping process: (a) binder closure; (b) die closure (Shih et al., 2009).

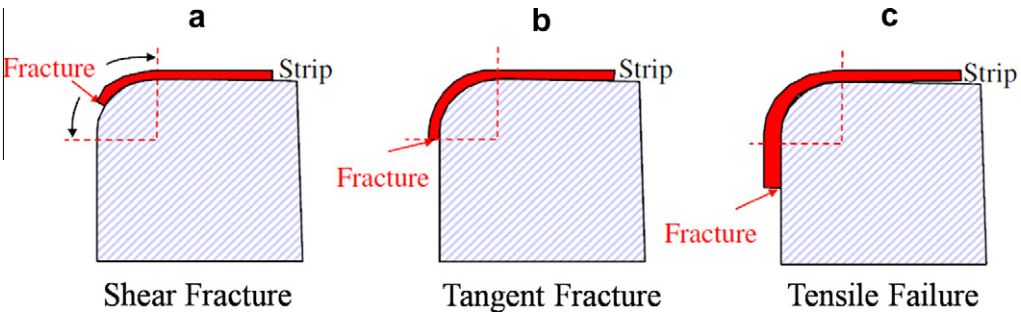

Fig. 10. Three typical failure modes/locations observed in a SFS test (Shih et al., 2009).

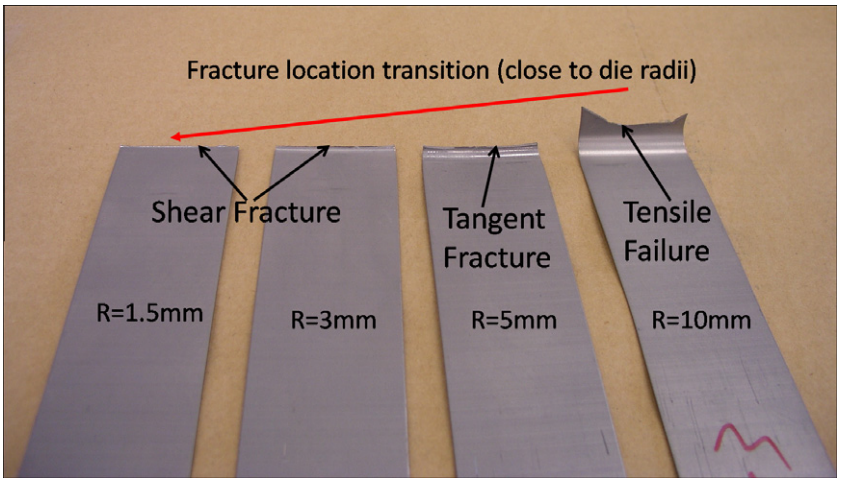

Fig. 11. Fractured DP780 specimens after SFS tests with four different lower die radii.

(50.8 mm) DP780 strips are utilized to validate our material modeling, especially the fracture predicting capability of the phenomenological fracture model proposed in Section 3. All strip specimens for this study were sheared perpendicular to the rolling direction from the same DP780 sheet. Each specimen is deburred before the test using a fine file instead of a mechanical deburrer to limit imperfections on the edge. The quasi-static SFS tests were performed with a constant upper die speed of 0.25 m/min, a fixed clamping distance d of 460 mm, total clamped strip length l of 600 mm and radii gap δ of 2 mm (Fig. 8). Teflon® fluoropolymer film is used to reduce friction between strips and dies.

It noteworthy that the upper die speed adopted in this study (0.25 m/min) is much lower than typical industrial forming practices. Such choice was made in order to minimize the effects of rate sensitivity and thermal softening on both plasticity and fracture, and thus focus on the intrinsic mechanics and fracture phenomenon during stretch-bending. Moreover, the lower loading rate would be more consistent with our plasticity and fracture calibration under quasi-static conditions. Nonetheless, the rate sensitivity and thermal softening effects are important topics especially when the drawing speed is high. Extensive studies have been done on the strain rate and temperature effects on stretch forming processes, e.g. Wagoner et al. (2009) and Kim et al. (2009). For the present material, the effect of loading rate (upper die speed) in SFS tests was also investigated experimentally by Shih (2009) and Shih et al. (2009). However, those data will not be analyzed in the present paper which focuses on quasi-static and isothermal conditions.

Four different lower die radii, 1.5 mm, 3 mm, 5 mm, 10 mm, were adopted for the SFS testing, and every strip specimen was tested all the way to fracture. Three tests were performed for each R/t condition, and the repeatability of the results was quite good. For each condition, the fracture location is repeatable. Meanwhile, the average coefficients of variation for wrap angle and wall stress at failure are both less than 2%, and detailed information about the data spread for each R/t condition is reported by Shih and Shi (2008) and Shih (2009). In this study, the tests that yield median drawing depth values for each condition were employed and compared with simulations in the following sections.

Photographs of typical fractured strips for each lower die radius are shown in Fig. 11. One can see a clear transition of fracture location from sidewall to die radius and fracture mode from tensile failure to shear fracture as the die radius decreases. This phenomenon is an important criterion for the validation of numerical simulations in Section 5 of this paper. Furthermore, the wall stress and wrap angle at the onset of failure as well as the load displacement response of the upper die for all R/t values are also compared with the numerical simulations in Section 5.

5. Numerical modeling and validation

In order to validate the present plasticity and fracture model for DP780 and investigate the applicability of these models to practical AHSS forming problems, detailed numerical simulations of the SFS tests are performed. The simulation results are compared with experiments and discussed in various aspects.

5.1. Model description

All the numerical simulations of the present SFS tests were performed in the environment of Abaqus Explicit (2009) with both Hill'48 plasticity and MMC fracture model implemented as a user

material subroutine (VUMAT). The element deletion technique is used to model the fracture process.

In numerical modeling of the stretch-bending operations, both three-dimensional (3D) finite element model (Kim et al., 2009) and plane strain finite element model (Bai and Wierzbicki, 2008) have been used in the literature, while shell element models are extensively employed in metal forming simulations. In this study, three models employing 3D, plane strain and shell elements, respectively, were built in Abaqus in an attempt to examine their applicability to this type of problem, see Fig. 12. All the model geometries and boundary conditions follow exactly their counterparts in the DP780 SFS tests described in Section 4. For 3D and shell element models, the symmetry condition in the width direction was utilized to save computational time.

In these three models, the tools, including an upper die, a lower die and a lower binder (Fig. 12a), are represented by analytical rigid surfaces in Abaqus. The detailed information about three finite element models is listed in Table 4. It should be noted that the friction coefficient in Table 4 is determined by an inverse method. A series of simulations with different friction coefficients were carried out using the shell element model for the $R/t = 5$ case, and

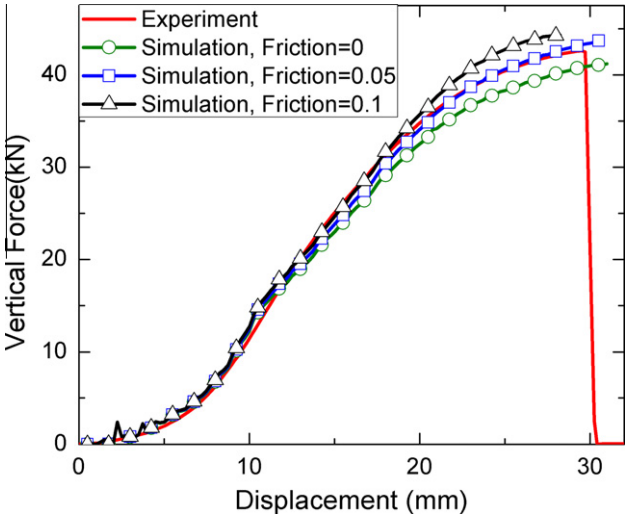

Fig. 13. Comparison of upper die load–displacement responses of simulations with different friction coefficient against experimental data.

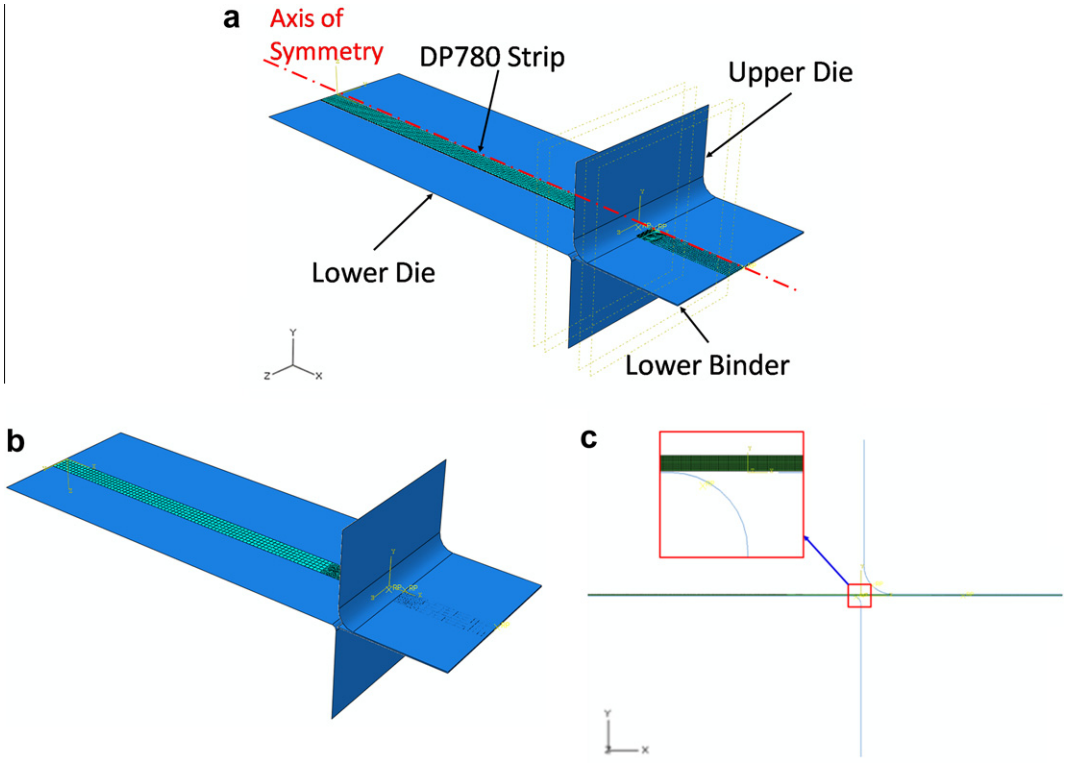

Fig. 12. Numerical models of the SFS test with different element type: (a) 3D element model; (b) shell element model; and (c) plane strain element model.

Table 4
Summary of computational information about three FE models.

	3D Element model	Shell element model	Plane strain element model
Element type (Abaqus)	C3D8R	S4R	CPE4R
Mesh size (critical area)	0.2 mm × 0.2 mm × 0.2 mm	1 mm × 1 mm	0.1 mm × 0.1 mm
Total number of elements	52,310	3205	9932
Number of through thickness integration points (critical area)	5	5	10
Solver	Abaqus Explicit 6.9-1		
Contact algorithm	Penalty contact method		
Friction coefficient	0.05 (between all contact surfaces)		

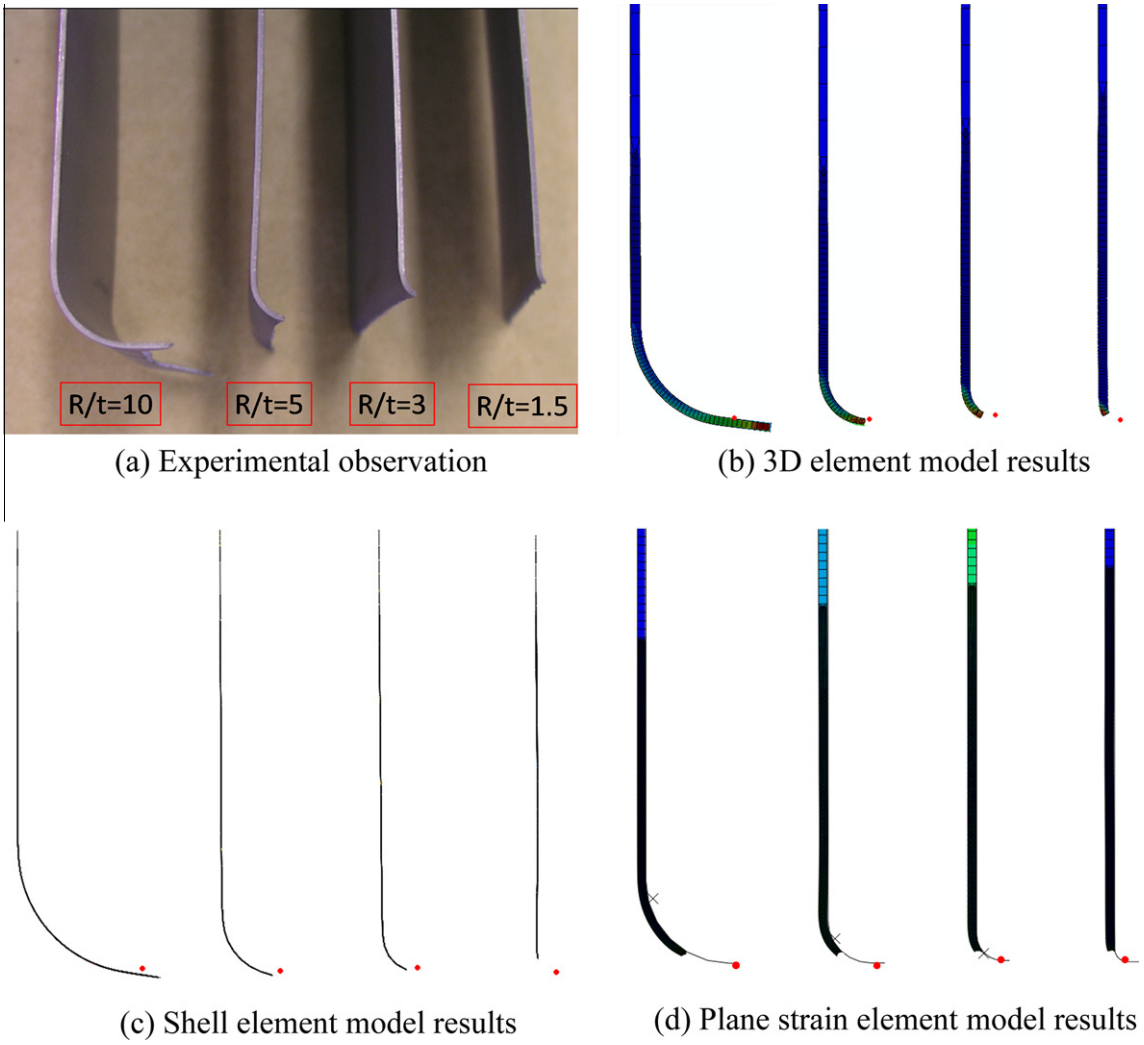

Fig. 14. Comparison of the fractured strips observed in tests against the simulation results.

the vertical force versus displacement responses of the upper die are compared with the test result in Fig. 13. It can be seen that the friction coefficient 0.05 provides best correlation, and the low value is in accordance with the fact that Teflon® film was used as lubricant during tests.

5.2. Results and validations

Twelve simulations were performed using the three models featuring different element types. For each model, four simulations with different values of lower die radius R were carried out in order to predict the fracture location transitions as shown in Fig. 11, as well as the upper die load–displacement response, wrap angle and wall stress at the onset of failure for each R/t value. The four lower die radii adopted in the simulations are 1.5 mm, 3 mm, 5 mm and 10 mm, which are the same as in the experiments, and corresponds to R/t ratios 1.5, 3, 5 and 10, respectively, for the sheet thickness 1 mm.

5.2.1. Fracture location/mode

Referring to Fig. 10, there are three typical fracture locations observed in the SFS tests, and the R/t ratio is an important factor that influences the transition between these locations. Fig. 11 clearly demonstrates the fracture mode shifting from shear fracture on the lower die radius to the tensile failure on sidewall as the R/t ratio increases.

In this section, the fracture location/mode transition is studied through numerical simulations. The fractured upper halves of the strips in all four tests are displayed in Fig. 14a, and it can be seen that tensile failure at sidewall occurs when R/t is 10, shear fractures on lower die radii show up when R/t are 3 and 1.5, while a mixed failure around tangent point happens when R/t is 5. The results form three FE models (after element deletion) are shown in Fig. 14b–d and compared with the experimental observation (Fig. 14a). In Fig. 14b–d, the red[4] dots denote the tangent point of the lower die. Apparently, the 3D element model and the shell element model can predict the fracture locations and the fracture mode transition accurately, while the plane strain element model always predicts fracture on the radii and is not able to describe the shift in the fracture location as the R/t ratio changes.

5.2.2. Upper die load–displacement response

During a SFS test, as the upper die moves downward and draws the strip into the die cavity, the vertical reaction force on the upper die increases, and its load–displacement responses were recorded

[4] For interpretation of the references to color in Fig. 14, the reader is referred to the web version of this paper.

for each test. The upper die load–displacement responses calculated by three FE models are compared in Fig. 15 with the experimental data for all four R/t ratios. The displacements at which the force drops corresponds to the drawing depth h at failure (Fig. 9b).

The correlation of the load–displacement curves is a good validation of both plasticity model and the fracture model. A good plasticity model enables the ideal correlation of the curve shape up to the point of fracture, and a good fracture model ensures

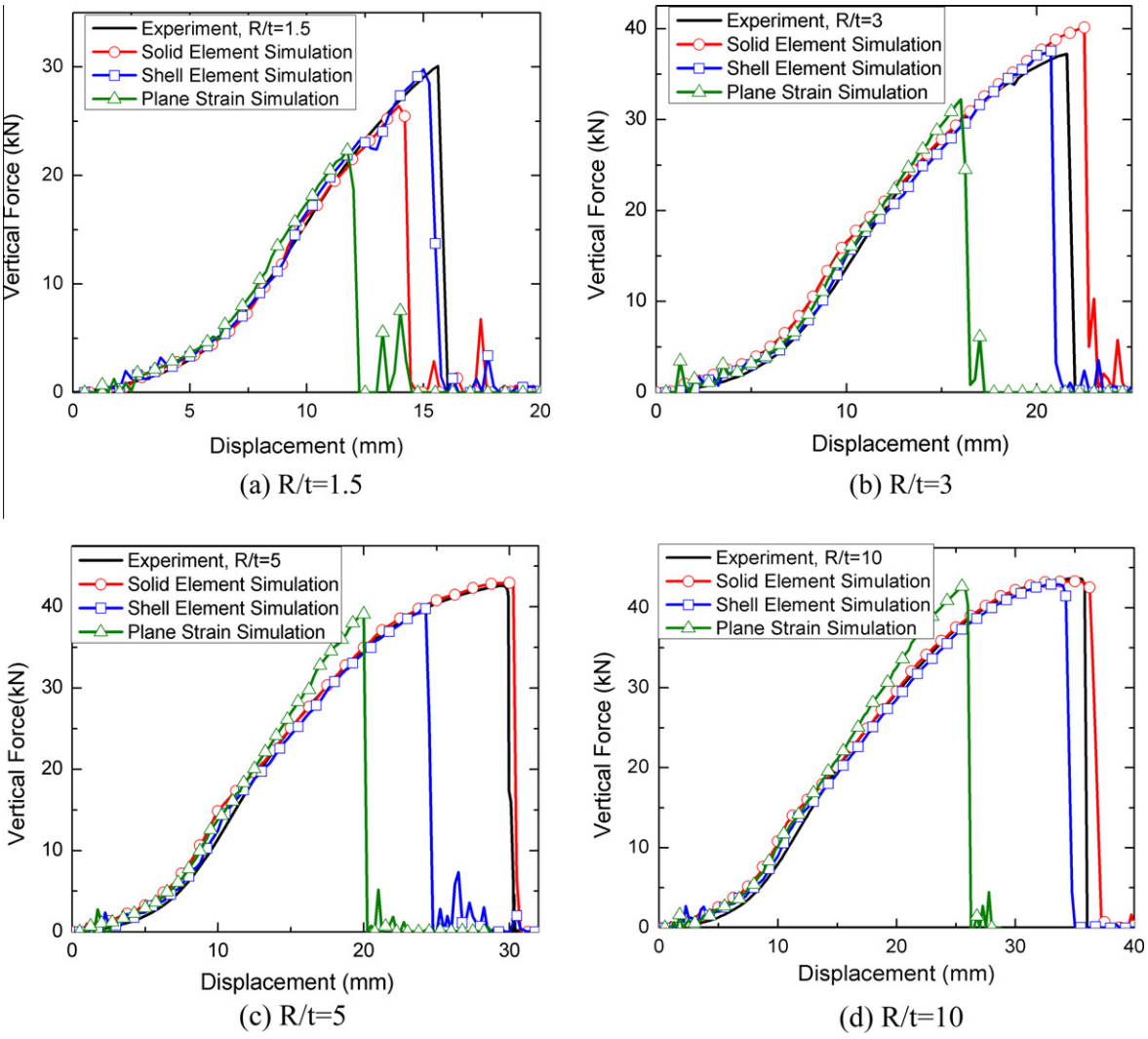

Fig. 15. Comparison of the upper die vertical force versus displacement curves between simulation results and experimental data for all R/t ratios.

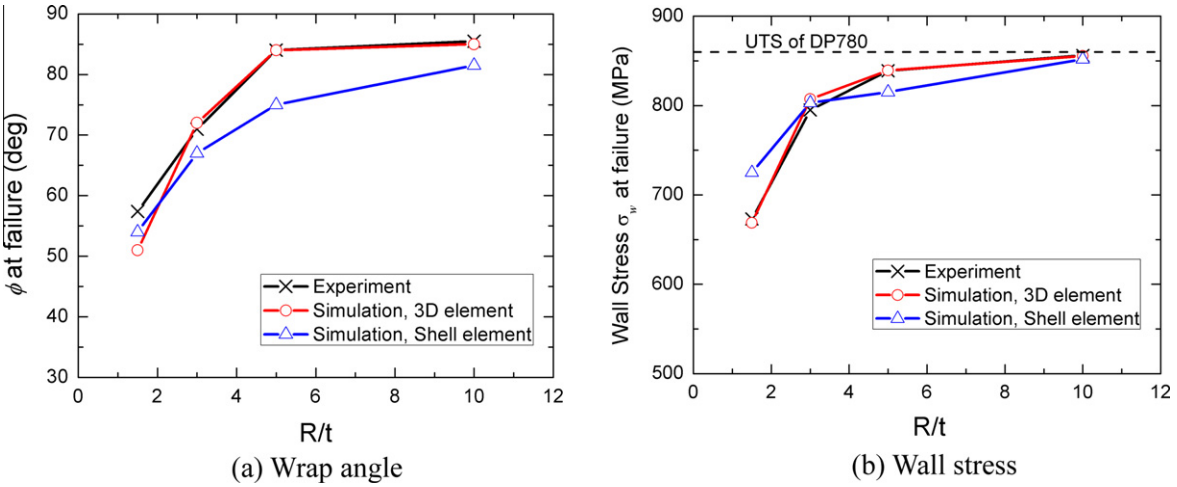

Fig. 16. Comparison of wrap angles and wall stresses at failure from simulation against experimental data.

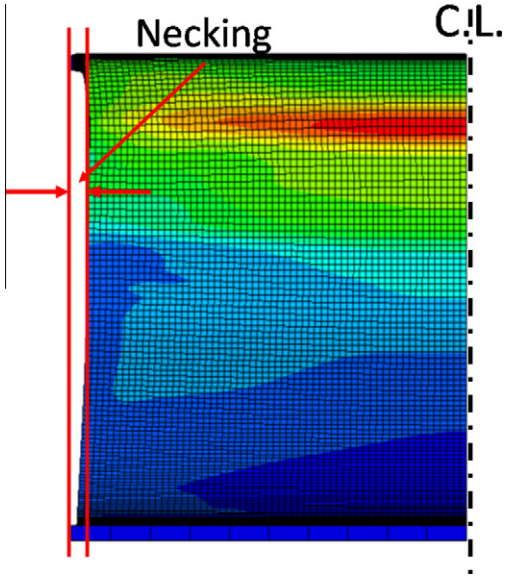

Fig. 17. Diffuse necking in width direction observed in the simulations (R/t = 5), and contour of the equivalent plastic strain indicates a localized necking.

the force dropping at right time. From Fig. 15, it is found that the 3D element model predicts the load–displacement curves for all four cases with good accuracy, the maximum error in drawing depth prediction is about 6% for R/t = 1.5. The shell element model predicts the shear fracture cases (R/t = 1.5 and 3) and the tensile failure case (R/t = 10) accurately, but it underestimates the drawing depth for the tangent failure case (R/t = 5) by about 15%. The plane strain element model predicts much earlier fracture for all cases, and provides poor load–displacement curve shape correlation for R/t value 5 and 10.

5.2.3. Wall stress and wrap angle

Besides the failure location and upper die load–displacement responses, the warp angle ϕ and wall stress σ_w at the onset of failure are also of great interest to the forming community. These two parameters are usually utilized to determine a critical R/t ratio below which shear fracture on die radii will occur (Walp et al., 2006; Shih and Shi, 2008; Shih et al., 2009). In both experiments and simulations, the wrap angles ϕ were calculated from drawing depth h at failure using trigonometry. Readers are referred to Appendix A for details. Based on the geometric relationship shown in Fig. 9b, the wall stress σ_w can be expressed in terms of the vertical force on upper die F_y, wrap angle ϕ and the original strip cross-sectional area A_0 as

$$\sigma_w = \frac{F_y}{A_0 \sin(\phi)} \tag{18}$$

Since the incompetence of plane strain model has been proved by Sections 5.2.1 and 5.2.2, here we limit our attention to the 3D and shell models. The wrap angle and wall stresses at the onset of failure were extracted from every 3D and shell simulation when the first element was deleted, and the results are compared with experimental data in Fig. 16. It can be seen that both 3D and shell element models can qualitatively predict the increase of ϕ and σ_w at failure as R/t value goes up. However, quantitatively, the 3D element model provides much better prediction for both ϕ and σ_w under most cases. It is noteworthy that the critical R/t ratio is often determined by observing the experimental curves shown in Fig. 16, and a dramatic change in the slope is usually a sign of the critical R/t value, which is around 5 for the present case. It should also be noted that the wall stress approaches the Ultimate Tensile Strength (UTS) of the present material as R/t increases, and this is also an evidence of the transition from shear fracture to tensile failure at high R/t value.

5.3. Discussions

By comparisons of simulation results against experimental data from various aspects, the accuracy of the present fracture modeling framework and its applicability to real forming problems have been validated. It has been found that the 3D element model provides best agreement with experiments on all aspects; including fracture locations, load–displacement responses, as well as specific wrap angles and wall stresses at failure. Shell element model predicts the fracture locations and upper die load–displacement responses with good accuracy, and can describe the transition trend of the wrap angle and the wall stress qualitatively but not quantitatively. The drawing depth, wrap angle and wall stress under transitional conditions (R/t = 3 and 5) could not be predicted as accurately as the 3D model. Nonetheless, considering its efficiency, the performance of the shell element model is also acceptable. As of the plane strain element model, it fails to predict the fracture location shifting (Fig. 14d) and significantly underestimates the drawing depth (Fig. 15). The reason is that the strip is not under strict plane strain especially when the tension level on the side wall gets high, and considerable necking in the width direction has been observed as shown in Fig. 17. Hence, the plane strain condition adds too much constraint to the model and makes the failure earlier.

5.3.1. Stress states at critical elements

Since the present fracture modeling is based on a stress state dependent fracture envelope, a close look into the evolution of

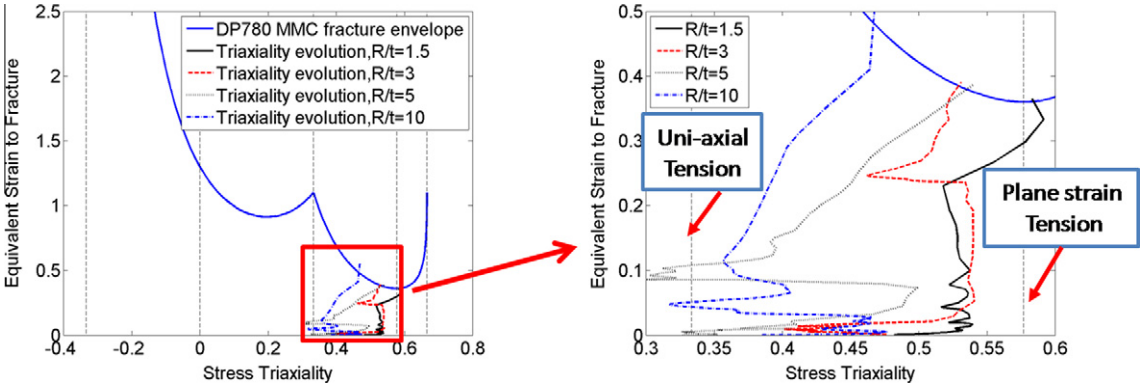

Fig. 18. Evolution of stress triaxiality on critical elements under four R/t values.

stress state at a critical material point could help better understand the fracture process. The stress triaxiality evolutions of the critical element (the point where fracture initiates) for all four cases with different R/t values were extracted from the 3D element model, and the triaxiality versus equivalent plastic strain curves were superimposed on the plane stress fracture envelope (Fig. 6b), as displayed in Fig. 18. It can be seen that the critical material point is experiencing a complex history of stress states, which calls for a stress state dependent fracture model. Meanwhile, Fig. 18 also indicates that the stress state gets closer to uniaxial tension as the R/t value increases, while approaches plane strain tension as R/t value goes down. Therefore, from a local point of view, the shear fracture at tight die radii is under plane strain condition, which features a lower fracture strain. It should also be noted that a full 3D fracture envelope (Fig. 6a) is implemented into the FE models, so the evolution of Lode parameter is also complicated and important, but only the stress triaxiality history is shown here due to paper length limit.

5.3.2. Sequence of damage accumulation

The stretch-bending operation is a complicated process, and many factors including R/t ratio, tension level and friction coefficient all have influence on the failure mode and location. Hence, it would be quite helpful to develop a generalized 'road map' of the damage evolution and fracture process. Recall that our proposed fracture model is Eq. (17), where D is a damage indicator, and fracture initiates when $D = 1$. Here, the distribution of D on the critical part of the strip (between two dies) is studied for $R/t = 10$. In this case, fracture initiation occurs the latest among all cases and the strip is experiencing a complex damage pattern before fracture. The 3D element model is used and a generalized sequence of damage accumulation is summarized as follows.

(i) Phase 1

As shown in Fig. 19a, in the beginning of the stretch-bending process, the damage is concentrated on the die radius. In this stage, the tensile level is low and the damage is mostly due to bending. Therefore, shear fracture will initiate in phase 1 if R/t value is small. For the present DP780 sheet, when R/t equals to 1.5 and 3, fracture occurs in this phase.

(ii) Phase 2

As drawing depth increases, the tensile level goes up, and the damage around die radius is caused by both bending and stretching. Since the friction restricts the tensile level in the strip portion which is in contact with the die radius, the damage concentration will move to the tangent area where both tension and bending level are high. For this study, fracture initiates in this phase when $R/t = 5$.

(iii) Phase 3

There are two competing damage concentration zones, one in tangent area and the other one on side wall. The reason for the shifting from phase 2 to phase 3 is that the contact friction again restricts the tensile level at the tangent area while the tensile level at the side wall gets high as draw depth keeps increasing. For this study, no fracture was observed in this phase.

(iv) Phase 4

As shown in Fig. 19d, if fracture does not occur during the first three phases, the damage will concentrate on the side wall as the upper die keeps moving downward. The contact friction will

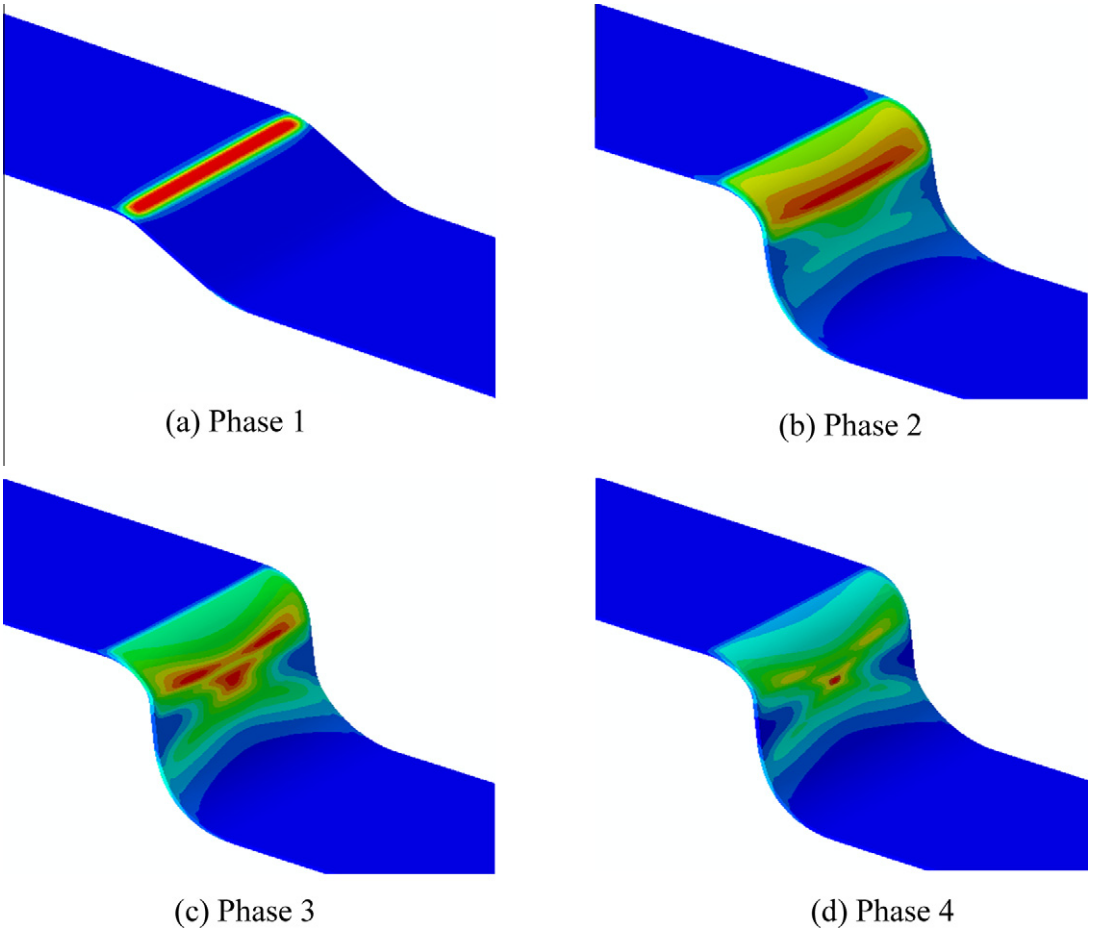

Fig. 19. Typical sequence of damage accumulation during a stretch-bending operation, color coded is damage indicator D. (For interpretation of the references to color in this figure legend, the reader is referred to the web version of this paper.)

restrict the tensile level on the tangent area and makes it much smaller than that of side wall. In this phase, tensile strain will be the main contribution to the damage, so fracture initiates in this phase is mostly tensile failure. For the present case, fracture happens in this phase when $R/t = 10$.

As analyzed above, fracture could happen in any of the four phases, and the damage level in each phase depends on R/t ratio, contact friction, tension level and the fracture envelope of the material. An in-depth understanding of the damage accumulation sequence would help us explain many phenomena observed in the stretch-bending operations but never interpreted by the experimentalists.

6. Parametric study

In this section, the effect of several modeling parameters, including tension level, tooling friction, mesh size and the magnitude of MMC fracture envelope, on the fracture location and punch load–displacement response are studied. Here, attention is limited to the 3D element model.

6.1. Effect of tension level

The tension level in the SFS test could be altered by changing the clamping distance d shown in Fig. 8. The baseline model used in this study is with $R/t = 10$, and the clamping distance d is 460 mm, same as in the test. Two additional simulations with a clamping distance of $d = 300$ mm and $d = 165$ mm were carried out to investigate the effect of tension level. Apparently, the smaller the clamping distance is, the higher the tension level in the strips will be.

As shown in Fig. 20, the location of fracture initiation shifts from the side wall to tangent area as the tension level increases. With reference to the foregoing discussion, fracture in the baseline case occurs in phase 4, the fracture in higher tension case ($d = 300$ mm) initiates in phase 3, and when the tension level is highest ($d = 165$ mm) fracture starts in phase 2. Therefore, a higher tension level in the strips can cause the fracture initiation earlier, and this is also demonstrated in Fig. 21. The reason is that a higher tensile force accelerates the damage accumulation by boosting tensile strain. The findings about tension level effect in the present numerical study agree well with published experimental observations (Shih and Shi, 2008; Shih et al., 2009; Shih, 2009) on a similar material.

6.2. Effect of tooling friction

The contact friction between the strip specimen and the die surfaces has great influence on the damage accumulation process. In this section, the base scenarios are the cases with R/t ratio 10 and baseline friction coefficient $\mu = 0.05$ as determined in Section 5.1. Three additional simulations with friction coefficient μ of 0, 0.03 and 0.1, respectively, were performed to study the friction effect on fracture location and the upper die load–displacement response.

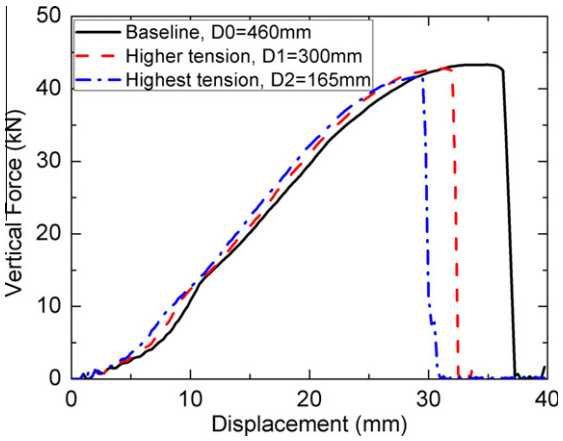

Fig. 21. Effect of strip tension level on the upper die load–displacement responses.

As shown in Fig. 22, the transition of fracture location from the side wall to the tangent area occurs as the friction coefficient decreases. One can see a clear phase 4 fracture when μ equals 0.05 and 0.1, a typical phase 3 fracture as μ reduces to 0.03, and a phase 2 fracture in the tangent area under frictionless condition. The contact friction could restrict the strip on die radii, hinder the development of large tensile strain in that region, and hence expedite the transition between phases shown in Fig. 19. Shih et al. (2009) observed the same trend through experiments with different lubricant on a similar material. Meanwhile, Fig. 23 indicates that the drawing depth at failure increase as friction decreases, and the explanation would be that a higher friction will bring about a shorter effective length under tension and thus a smaller elongation.

6.3. Effect of mesh size

In this section, studied is the effect of mesh size on the fracture location and upper die load–displacement response in the 3D element simulation in the case with $R/t = 5$. As shown in Table 4, the edge length of the elements in critical area in the baseline model is 0.2 mm, and the aspect ratio is 1:1:1. Here, three additional models with critical element edge length of 0.33 mm, 0.5 mm and 1 mm were built, and the critical element aspect ratio was kept to be

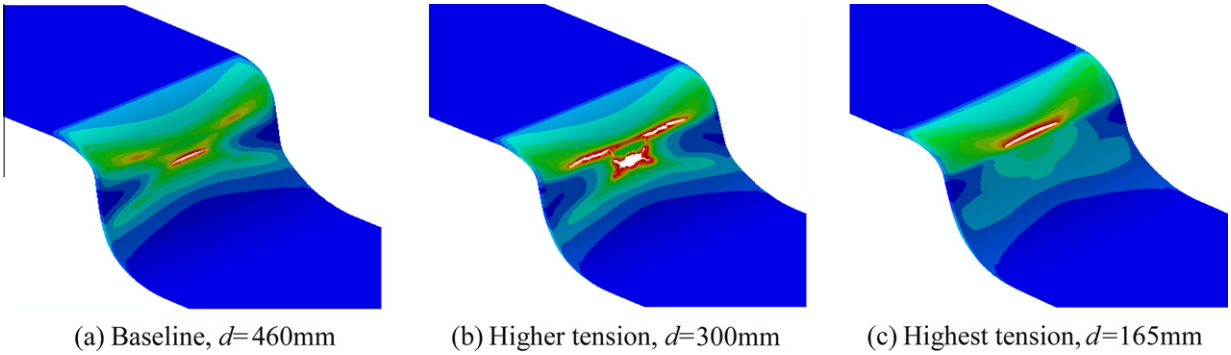

Fig. 20. Fracture initiation location shifts to die radii as tension level increases (contoured is damage indicator D).

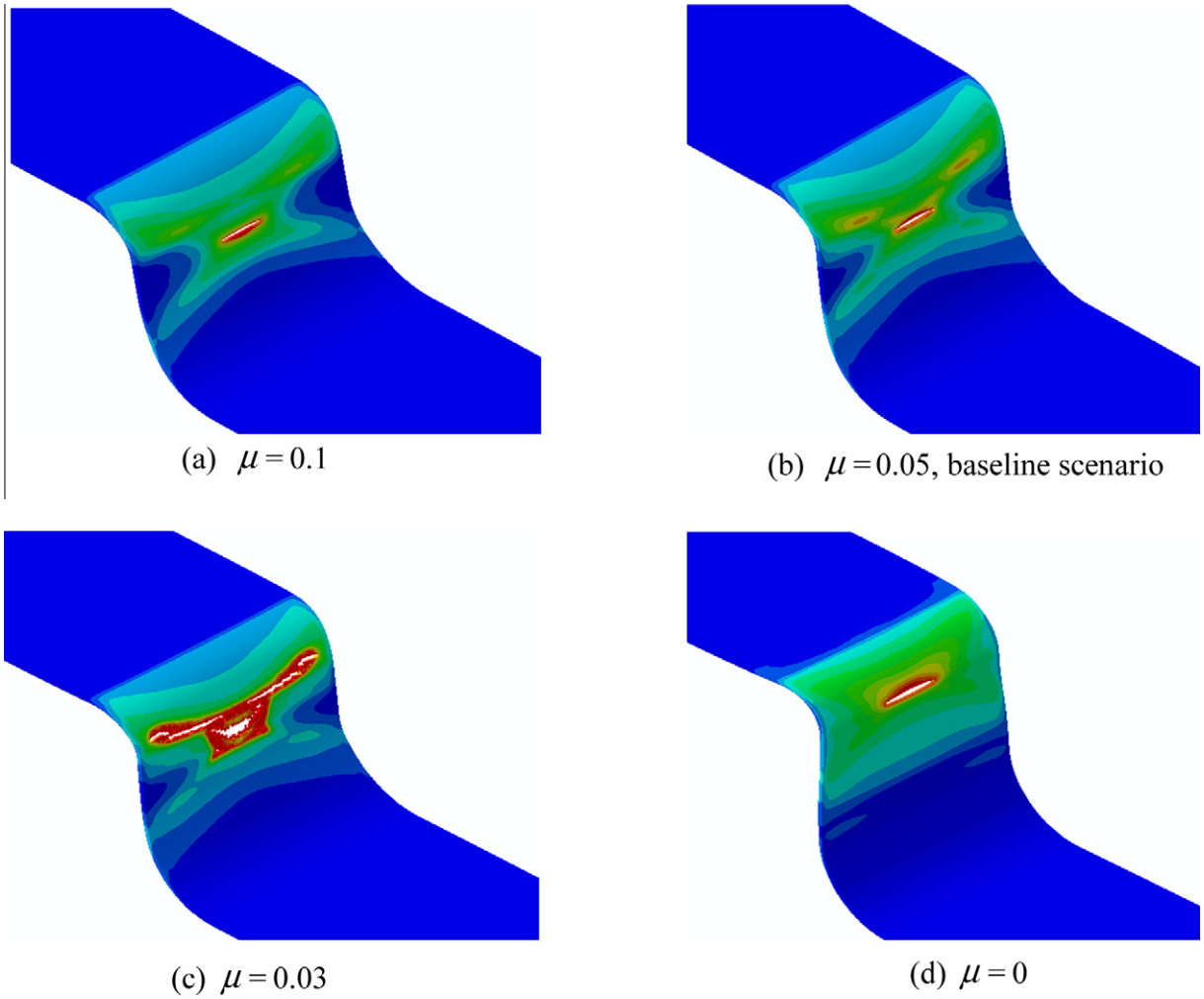

Fig. 22. Fracture location transition from side wall to die radii as contact friction decreases (contoured is damage indicator *D*).

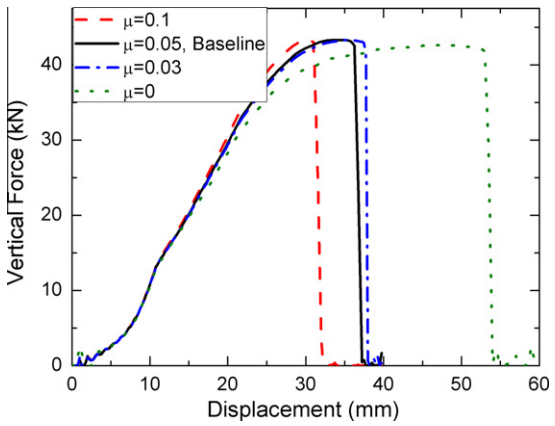

Fig. 23. Effect of contact friction coefficient on the upper die load–displacement response.

1:1:1. Fig. 24 shows that the fracture location in this case seems to be independent of mesh size, at least for the mesh size range we studied, the fracture always initiate in tangent area (phase 3) as in the test. The upper die load–displacement curve is shown in Fig. 25, and it indicates that the fracture initiation is delayed as the mesh gets coarser, and it converges to the experimental results as the mesh gets finer. However, mesh size effects always exist as long as the constitutive model does not have a characteristic length parameter, and local strain and damage accumulation usually change as mesh size varies. The details of mesh size effect are out of the scope of the present paper, but a simple way to reduce the mesh size effect is to keep a consistent length scale in fracture calibration and simulations. This length scale includes the reference length when measuring fracture strain using DIC, the mesh size when obtaining fracture strain using inverse method and the mesh size in numerical applications. The DIC reference length that resembles FE mesh size was set to be approximately 0.3 mm in this study, while the solid element sizes used for fracture calibration range from 0.15 mm to 0.3 mm due to different specimen geometries.

6.4. Effect of MMC fracture envelope

Due to the inevitable errors in the measurement of the fracture strain and the notorious mesh size effect, there is no such thing as the exact MMC fracture strain envelope, which is used as a reference strain level for damage accumulation. In this section, the effect of the fracture envelope magnitude on the present stretch-bending fracture problem is investigated. The magnitude of the fracture envelope is controlled by multiplying the baseline envelope shown in Fig. 6b with a scale factor k. As shown in Fig. 26,

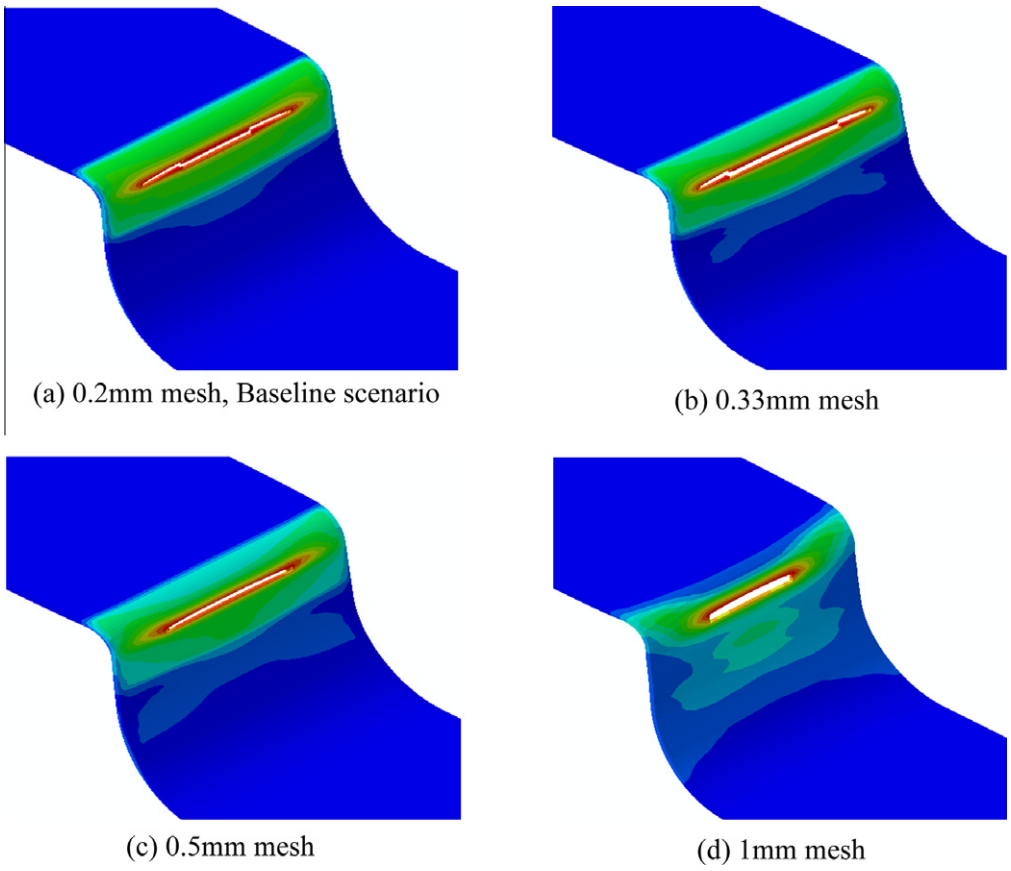

Fig. 24. Fracture initiation location unaltered for all four element sizes (contoured is damage indicator D).

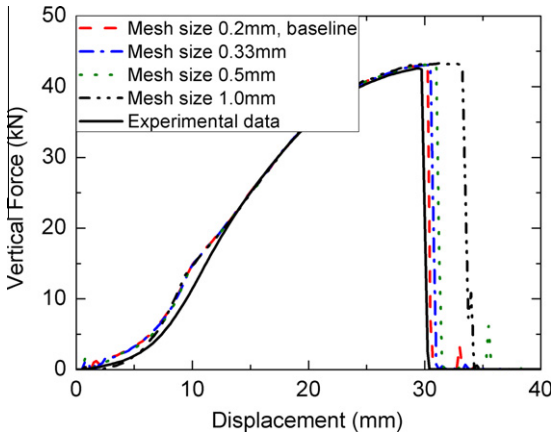

Fig. 25. Effect of mesh size on the upper die load–displacement response.

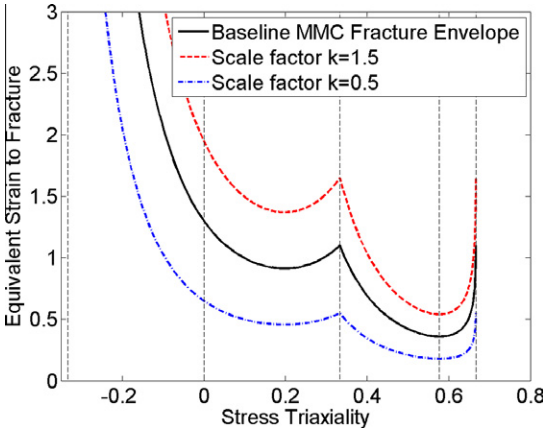

Fig. 26. Two additional fracture envelopes obtained by scaling the original envelope.

two additional scenarios with k values 0.5 and 1.5 are considered in order to study the effect of fracture envelope.

Here, the fracture envelope effect on two cases, with R/t ratio of 10 and 1.5, is studied. As of the fracture location, the height of the fracture envelope has little influence on the $R/t = 1.5$ case, because the radius is so tight that bending strain is always dominant and fracture always initiates in phase 1. For the $R/t = 10$ case, the fracture location shifts from side wall to tangent area as k reduces to 0.5, as shown in Fig. 25. A lower fracture envelope will accelerate the damage accumulation, and thus cause the transition of fracture initiation from phase 4 to phase 3. As of the upper die load–displacement response, the effect of the fracture envelope is more significant on the $R/t = 1.5$ case than the $R/t = 10$ case, as shown in Fig. 27. The reason for this phenomenon is that the tensile failure under $R/t = 10$ case features larger localization than the shear fracture for $R/t = 1.5$ case. The evolution of equivalent plastic strain at the critical element (the first element deleted) is also superimposed in Fig. 28, from which one can clearly see more significant strain localization in $R/t = 10$ case than that of $R/t = 1.5$ case.

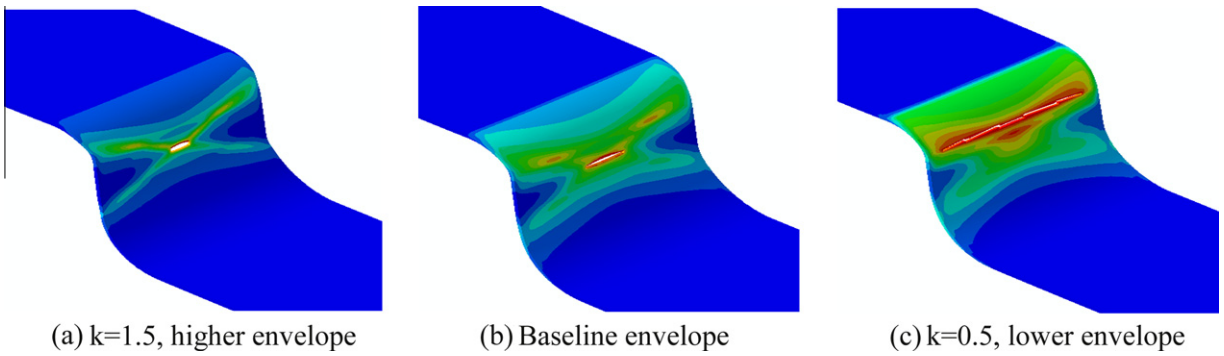

Fig. 27. Fracture location transition from side wall to die radii as fracture envelope diminishes for $R/t = 10$ (contoured is damage indicator D).

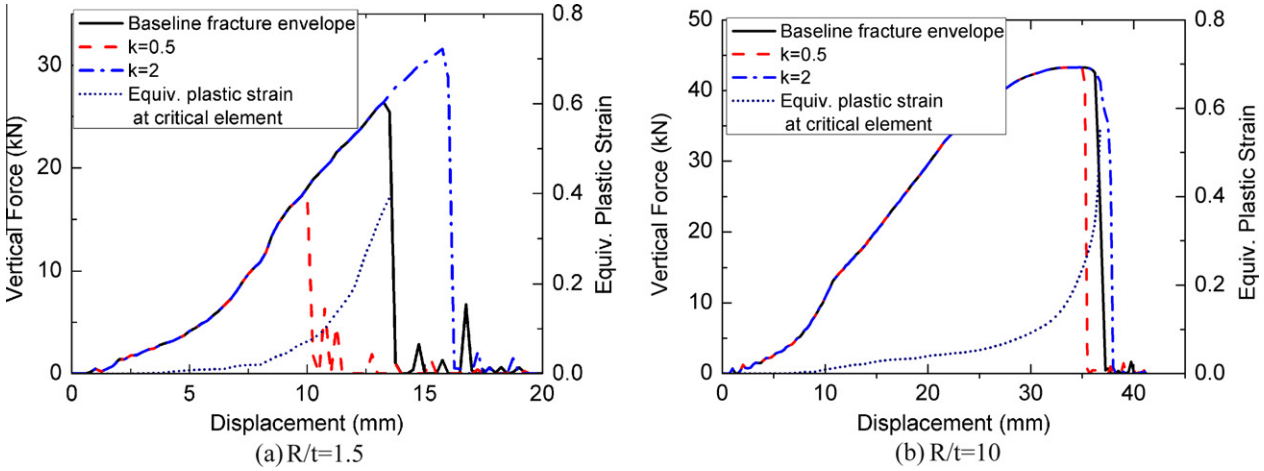

Fig. 28. The upper die load–displacement curves under three different fracture strain envelope with superimposed equivalent plastic strain versus upper die displacement curve.

7. Conclusions

In this paper, a recently developed phenomenological MMC ductile fracture model (Bai and Wierzbicki, 2010), which features both pressure sensitivity and Lode angle dependence, is employed to predict failures in a stretch-bending operation on AHSS sheets. From a number of tests performed on various types of specimens, both plasticity and ductile fracture of the present DP780 sheet has been fully characterized. Detailed finite element models with three different element types have been built for the present quasi-static SFS test, and the applicability and accuracy of the present plasticity and fracture models on a type of practical forming processes under isothermal condition have been validated. The key conclusions from this study are:

(1) The Hill's (1948) yield function, together with its associated flow rule and a carefully calibrated hardening law is able to describe the plastic behavior of the present material accurately. Meanwhile, the MMC fracture envelope, which is highly nonlinear in the $(\eta, \bar{\theta}, \hat{\varepsilon}_f)$ space, fits the experimental fracture data with very good accuracy.

(2) By comparing the numerical results and experimental data (Shih and Shi, 2008; Shih et al., 2009; Shih, 2009) of the SFS tests, it has been found that the 3D element model provides best prediction in all aspects including fracture location/mode, die load–displacement responses, failure wall stress and failure wrap angle. The performance of the shell element model is also acceptable considering its high efficiency. However, the plane strain element is not suitable for this problem, since considerable necking has been developed and plane strain condition adds too much constraint.

(3) A series of parametric study has been carried out with the 3D element model. It has been found that the experimentally observed effects of tension level and tooling friction can be accurately captured by the present model. Mesh size and the magnitude of fracture envelope both have influence on the damage accumulation process, but they have different impact on the fracture phenomena. For this study, mesh size of the 3D element model has little influence on the fracture location, and the load–displacement response is converged as mesh gets finer. The fracture envelope has larger influence on the drawing depth for tighter radii case, while it could shift the fracture location in the larger radii case. A typical damage accumulation process has been summarized in this paper and has been found useful in analyzing the effect of various parameters.

Acknowledgements

The support of this work comes from the MIT/Industry AHSS Fracture Consortium. US Steel Corporation is gratefully acknowledged for providing the material and experimental data. Thanks are also due to Dr. M. Shi, Dr. M. Chen, Dr. H. Shih and Dr. A. Konieczny from US steel for valuable discussions.

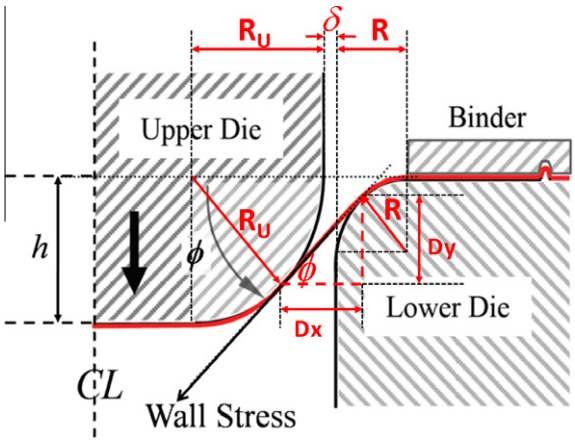

Fig. A1. Geometric representation of stretch-bending process.

Appendix A. Trigonometric calculation of wrap angle ϕ

As shown in Fig. A1, R, R_u and δ represent the lower die radius, the upper die radius and the die clearance, respectively, while ϕ and h denote the wrap angle and drawing depth h at failure. As drawing depth is easier to measure during tests, we want to derive an expression of ϕ in terms of h and other known quantities.

According to trigonometry, it is clear that

$$\tan\phi = \frac{D_y}{D_x} \tag{A1}$$

where D_y and D_x can be calculated from geometric relations as

$$D_y = h - R_u(1-\cos\phi) - R(1-\cos\phi) \tag{A2}$$

$$D_x = R_u(1-\sin\phi) + R(1-\sin\phi) + \delta \tag{A3}$$

Substitute Eqs. (A2) and (A3) back into Eq. (A1), one can obtain

$$\tan\phi = \frac{h - R_u(1-\cos\phi) - R(1-\cos\phi)}{R_u(1-\sin\phi) + R(1-\sin\phi) + \delta} \tag{A4}$$

This is a nonlinear trigonometric function of ϕ. Given, h, R_u, R and δ, Eq. (A4) can be easily solved using mathematical software, e.g. Matlab.

References

Abaqus, 2009. Reference Manuals v6.9. Dassault Systèmes Simulia Corp.

Bai, Y., 2008. Effect of loading history in necking and fracture, Ph.D. Thesis, Massachusetts Institute of Technology.

Bai, Y., Wierzbicki, T., 2008. Predicting fracture of AHSS sheets on the punch and die radii and sidewall. In: Proceedings of Numisheet 2008, Interlaken, Switzerland, pp. 297–306.

Bai, Y., Wierzbicki, T., 2010. Application of extended Mohr–Coulomb criterion to ductile fracture. International Journal of Fracture 161, 1–20.

Banu, M., Takamura, M., Hama, T., Naidim, O., Teodosiu, C., Makinouchi, A., 2006. Simulation of springback and wrinkling in stamping of a dual phase steel rail-shaped part. Journal of Materials Processing Technology 173, 178–184.

Bao, Y., 2003. Prediction of ductile track formation in uncracked bodies, Ph.D. Thesis, Massachusetts Institute of Technology.

Bao, Y.B., Wierzbicki, T., 2004. A comparative study on various ductile crack formation criteria. Journal of Engineering Materials and Technology – Transactions of the ASME 126, 314–324.

Barlat, F., Brem, J.C., Yoon, J.W., Chung, K., Dick, R.E., Lege, D.J., Pourgoghrat, F., Choi, S.H., Chu, E., 2003. Plane stress yield function for aluminum alloy sheets. Part 1: theory. International Journal of Plasticity 19, 1297–1319.

Beese, A.M., Luo, M., Li, Y., Bai, Y., Wierzbicki, T., 2010. Partially coupled anisotropic fracture model for aluminum sheets. Engineering Fracture Mechanics 77, 1128–1152.

Benzerga, A.A., Besson, J., Pineau, A., 2004. Anisotropic ductile fracture. Part II: theory. Acta Materialia 52, 4639–4650.

Chaboche, J.L., 1988a. Continuum damage mechanics. 1. General concepts. Journal of Applied Mechanics – Transactions of the ASME 55, 59–64.

Chaboche, J.L., 1988b. Continuum damage mechanics. 2. Damage growth, crack initiation, and crack-growth. Journal of Applied Mechanics – Transactions of the ASME 55, 65–72.

Chen, P., Koc, M., 2007. Simulation of springback variation in forming of advanced high strength steels. Journal of Materials Processing Technology 190, 189–198.

Clift, S.E., Hartley, P., Sturgess, C.E.N., Rowe, G.W., 1990. Fracture prediction in plastic-deformation processes. International Journal of Mechanical Sciences 32, 1–17.

Cockcroft, M.G., Latham, D.J., 1968. Ductility and the workability of metals. Journal of the Institute of Metals 96, 33–39.

Coppola, T., Cortese, L., Folgarait, P., 2009. The effect of stress invariants on ductile fracture limit in steels. Engineering Fracture Mechanics 76, 1288–1302.

Dunand, M., Mohr, D., 2010. Hybrid experimental–numerical analysis of basic ductile fracture experiments for sheet metals. International Journal of Solids and Structures 47, 1130–1143.

Durrenberger, L., Molinari, A., Rusinek, A., 2008. Internal variable modeling of the high strain-rate behavior of metals with applications to multiphase steels. Materials Science and Engineering A – Structural Materials Properties Microstructure and Processing 478, 297–304.

Gotoh, M., Katoh, M., Yamashita, M., 1997. Studies of stretch-drawing process of sheet metals. Journal of Materials Processing Technology 63, 123–128.

Gurson, A.L., 1975. Plastic flow and fracture behavior of ductile materials incorporating void nucleation, growth and interaction, Ph.D. Thesis, Brown University.

Hancock, J.W., Mackenzie, A.C., 1976. Mechanisms of ductile failure in high-strength steels subjected to multi-axial stress states. Journal of the Mechanics and Physics of Solids 24, 147–160.

Hasek, V., 1978. Untersuchung und theoretische Beschribung wichtiger Einflussgroessen auf das Grenzformaenderungsschaubild [Research and theoretical description concerning the influences on the FLDs (in German)]. Blech Rohre Profile 25, 213–220.

Hill, R., 1948. A theory of the yielding and plastic flow of anisotropic metals. Proceedings of the Royal Society of London Series A 193, 281–297.

Hudgins, A., Matlock, D., Speer, J., Fekete, J., Walp, M., 2007. The susceptibility to shear fracture in bending of advanced high strength steels. In: Proceedings of Materials Science and Technology (MS&T), Detroit, MI.

Issa, D.L., 2009. Testing and prediction of failure of AHSS sheets at die radius and sidewall using novel fracture apparatus, Master Thesis, Massachusetts Institute of Technology.

Johnson, G.R., Cook, W.H., 1985. Fracture characteristics of 3 metals subjected to various strains, strain rates, temperatures and pressures. Engineering Fracture Mechanics 21, 31–48.

Kim, J., Gao, X.S., Srivatsan, T.S., 2004. Modeling of void growth in ductile solids: effects of stress triaxiality and initial porosity. Engineering Fracture Mechanics 71, 379–400.

Kim, J.H., Sung, J.H., Wagoner, R.H., 2009. Thermo-mechanical modeling of draw-bend formability tests. In: Proceedings of IDDRG Conference, Golden, CO, pp. 503–512.

Leblond, J.B., Perrin, G., Devaux, J., 1995. An improved Gurson-type model for hardenable ductile metals. European Journal of Mechanics A – Solids 14, 499–527.

Lee, M.G., Kim, D., Kim, C.M., Wenner, M.L., Wagoner, R.H., Chung, K., 2005. Spring-back evaluation of automotive sheets based on isotropic-kinematic hardening laws and non-quadratic anisotropic yield functions. Part II: characterization of material properties. International Journal of Plasticity 21, 883–914.

Lemaitre, J., 1985. A continuous damage mechanics model for ductile fracture. Journal of Engineering Materials and Technology – Transactions of the ASME 107, 83–89.

Leroy, G., Embury, J.D., Edward, G., Ashby, M.F., 1981. A model of ductile fracture based on the nucleation and growth of voids. Acta Metallurgica 29, 1509–1522.

Levy, B.S., Van Tyne, C.J., 2009. Predicting breakage on a die radius with a straight bend axis during sheet forming. Journal of Materials Processing Technology 209, 2038–2046.

Li, Y., Luo, M., Gerlach, J., Wierzbicki, T., 2010. Prediction of shear-induced fracture in sheet metal forming. Journal of Materials Processing Technology, in press, doi:10.1016/j.jmatprotec.2010.06.021.

Luo, M., Wierzbicki, T., 2009. Ductile fracture calibration and validation of anisotropic aluminum sheets. In: Proceedings of 2009 SEM Annual Conference and Exposition on Experimental and Applied Mechanics, Albuquerque, NM, pp. 402–413.

Marciniak, Z., Duncan, J., 1992. Mechanics of Sheet Metal Forming. Edward Arnold, London, UK.

McClintock, F.A., 1968. A criterion of ductile fracture by the growth of holes. Journal of Applied Mechanics 35, 363–371.

Mohr, D., Ebnoether, F., 2009. Plasticity and fracture of martensitic boron steel under plane stress conditions. International Journal of Solids and Structures 46, 3535–3547.

Nahshon, K., Hutchinson, J.W., 2008. Modification of the Gurson model for shear failure. European Journal of Mechanics A – Solids 27, 1–17.

Oh, S.I., Chen, C.C., Kobayashi, S., 1979. Ductile fracture in axisymmetric extrusion and drawing. 2. Workability in extrusion and drawing. Journal of Engineering for Industry – Transactions of the ASME 101, 36–44.

Pardoen, T., Hutchinson, J.W., 2000. An extended model for void growth and coalescence. Journal of the Mechanics and Physics of Solids 48, 2467–2512.

Rice, J.R., Tracey, D.M., 1969. On the ductile enlargement of voids in triaxial stress fields. Journal of the Mechanics and Physics of Solids 17, 201–217.
Shih, H., 2009. An experimental study on shear fracture of advanced high strength steels. In: Presentations of Great Design in Steel 2009, Detroit, MI.
Shih, H.-C., Shi, M.F., 2008. Experimental study on shear fracture of advanced high strength steels. In: Proceedings of International Conference on Manufacturing Science and Engineering, MSEC 2008-72046.
Shih, H.-C., Shi, M.F., Xia, Z.C., Zeng, D., 2009. Experimental study on shear fracture of advanced high strength steels: part II. In: Proceedings of International Conference on Manufacturing Science and Engineering, West Lafayette, IN, MSEC 2009-84070.
Sriram, S., Wong, C., Huang, M., Yan, B., 2003. Stretch-bendability of advanced high strength steels. In: Proceedings of SAE 2003 World Congress, Detroit, MI, SAE 2003-01-1151.
Tvergaard, V., Needleman, A., 1984. Analysis of cup-cone fracture in a round tensile bar. Acta Materialia 32, 157–169.
Voyiadjis, G.Z., Dorgan, R.J., 2007. Framework using functional forms of hardening internal state variables in modeling elasto-plastic-damage behavior. International Journal of Plasticity 23, 1826–1859.
Wagoner, R., Kim, J., Sung, J., 2009. Formability of advanced high strength steels. International Journal of Material Forming 2, 359–362.
Walp, M.S., Wurm, A., Siekirk, J.F., Desai, A.K., 2006. Shear fracture in advanced high-strength steels. In: Proceedings of SAE 2006 World Congress, Detroit, MI, SAE 2006-01-1433.
Walters, C., 2009. Development of a punching technique for ductile fracture testing over a wide range of stress states and strain rates, Ph.D. Thesis, Massachusetts Institute of Technology.
Wierzbicki, T., Xue, L., 2005. On the effect of the third invariant of the stress deviator on ductile fracture. Technical Report 136, Impact and Crashworthiness Lab, Massachusetts Institute of Technology.
Xue, L., 2007a. Damage accumulation and fracture initiation in uncracked ductile solids subject to triaxial loading. International Journal of Solids and Structures 44, 5163–5181.
Xue, L., 2007b. Ductile fracture modeling: theory, experimental investigation and numerical verification, Ph.D. Thesis, Massachusetts Institute of Technology.
Yoshida, F., Uemori, T., Fujiwara, K., 2000. Elastic–plastic behavior of steel sheets under in-plane cyclic tension-compression at large strain. Proceedings of Symposium on Constitutive Equations and Their Role in Applied Deformation Behavior, vol. 18. Whistler, Canada, pp. 633–659.
Zhang, K.S., Bai, J.B., Francois, D., 2001. Numerical analysis of the influence of the Lode parameter on void growth. International Journal of Solids and Structures 38, 5847–5856.